Master Thesis

Influence of the ionomer content and dispersion solvent on the PEMWE performance and stability

carried out for the purpose of obtaining the degree of Master of Science (MSc), submitted at TU Wien, Faculty of Mechanical and Industrial Engineering, by

Benedikt Karan

Mat.Nr.: 01414319

under the supervision of

Univ.-Prof. Dipl.-Ing. Dr.-techn. Hermann Hofbauer

(Institute of Chemical, Environmental and Bioscience Engineering, E166)

and co-supervision of

Dr. Ivan Garcia-Torregrosa

(TNO, Netherlands Organisation for Applied Scientific Research)

Vienna, January 2021

I confirm, that going to press of this thesis needs the confirmation of the examination committee.

Affidavit

I declare in lieu of oath, that I wrote this thesis and performed the associated research myself, using only literature cited in this volume. If text passages from sources are used literally, they are marked as such.

I confirm that this work is original and has not been submitted elsewhere for any examination, nor is it currently under consideration for a thesis elsewhere.

I acknowledge that the submitted work will be checked electronically-technically using suitable and state-of-the-art means (plagiarism detection software). On the one hand, this ensures that the submitted work was prepared according to the high-quality standards within the applicable rules to ensure good scientific practice "Code of Conduct" at the TU Wien. On the other hand, a comparison with other student theses avoids violations of my personal copyright.

_____   _____
City and Date   *Signature*

Acknowledgements

First of all, I would like to thank the entire TNO staff of the "Biomass and Energy Efficiency" department in Petten (Netherlands) and especially Ivan Garcia-Torregrosa, who gave me the opportunity to write my thesis in this brilliant research institute and gave me an in-depth look at what it's like to work in applied research. Without his guidance, explanations and personal commitment, the thesis project would not have been possible on this scale and despite the exceptional circumstances of 2020. I would also like to thank him for letting me help design the scope of the experiment.

I am very grateful to my supervisor's team managed by Dr. Overwijk. It was indeed a truly challenging and rewarding time. I would especially like to thank Jakobert Veldhuis for his technical support with the laboratory set-up and his keen observation skills to remove any objectives during the laboratory work. A special thanks to Claire Ferchaud for her inspiring keen ideas and input. I am also very thankful to Xiaoqian Lu for the realisation of the SEM measurements. Many thanks to Mark Sillessen and Hans van Wees for their support in carrying out the electrolysis test series.

Furthermore, I would like to express my gratitude to Univ.-Prof. Dipl.-Ing. Dr.-techn. Hermann Hofbauer for being my internal supervisor and the allowance to do this thesis outside of the Vienna University of Technology. Without his commitment and guidance, the internship abroad would not have gone so smoothly. In general, thank you to all my professors and fellow students for inspiration and a great time. Without them I could not have pursued my passion to this extent. In particular I would like to thank Ass.Prof. Dipl.-Ing. Dr.techn. Mauschitz for his support and Univ. Prof. Dr. rer. nat. Fleig for fuelling my interest in technical electrochemistry.

Moreover, I would like to thank my study colleagues and professors I have met during my semester at the University of Antwerp as well. They encouraged me to do my master's thesis in another foreign country and were available all the time.

Last but not least, I would like to express my heartfelt gratitude to my parents for their valuable encouragement and support during my studies. I am very grateful for my siblings and friends for their advice and emotional support. Furthermore, I am especially thankful to my sister for proofreading and her advice. This accomplishment would not have been possible without them.

Table of Contents

Abstract

This study examines the effect of the ink composition onto the performance of the anodic catalyst layer (CL) in a proton exchange membrane water electrolyser (PEMWE). The corresponding membrane electrode assemblies (MEAs) are prepared on decals and subsequently hot-press transferred. The main objective is to enable effective long-term operation, while the used iridium amount is reduced and the remaining amount optimally utilised. The formulation of the inks used for the CL manufacturing are adjusted to achieve this objective and will enable the commercialisation of large-scale PEMWEs with increased mass activity. The main components of the ink are the catalyst material, the ionomer and the dispersion solvent. Both liquid components are systematically varied to improve the electrolysis performance. Rotating disk electrode (RDE) experiments are used for the comparison of supported catalyst materials in order to determine and compare the polarisation reactivity. An existing protocol based on previous proton exchange membrane fuel cell (PEMFC) research is originally used for the ink preparation of the screen-printed CLs. This protocol is modified to obtain optimised drying conditions, ideal ionomer contents as well as a beneficial selection of dispersion solvents for PEMWE inks.

The best performing anodic CL has a Nafion® content of 10 wt% in the dried CL, while a 50:50 mass ratio of the cyclohexanol/propylene glycol mixture is used for the ink formulation. This results in lower internal resistance due to more homogeneous dispersion of the unsupported iridium black (Ir black) catalyst powder. Finally, these improvements lead to a potential of 1.867 V @ 2 A/cm². The tested MEA has an Ir loading of 1.88 mg/cm² within the anodic CL. This results in the production of approximately 0.197 standard litres per minute (SLPM) of hydrogen for each cell with an active cell area of 10 cm².

Kurzfassung

Diese Studie untersucht den Einfluss der Tintenzusammensetzung auf die Leistung der anodischen Katalysatorschicht (CL) bei der Protonenaustauschmembran-Wasserelektrolyse (PEMWE). Die Membran-Elektroden-Einheiten (MEAs) werden auf Abziehfolien vorbereitet und anschließend im Heißpressverfahren übertragen. Das Hauptziel besteht darin, einen effektiven Langzeitbetrieb zu ermöglichen, wobei der Gehalt an Iridium reduziert und die verbleibende Menge optimal ausgenutzt werden soll. Die Formulierung der für die CL-Herstellung verwendeten Katalysator-Drucktinten werden auf dieses Ziel hin abgestimmt und ermöglichen dadurch die Kommerzialisierung von großformatigen PEMWEs mit erhöhter Massenaktivität. Die Hauptbestandteile der Drucktinten sind dabei das Katalysatormaterial, der Ionomer und das Dispersionslösungsmittel. Die beiden zuletzt genannten Komponenten werden systematisch variiert und untersucht, um die Elektrolyseleistung der MEA-Zelle zu verbessern. Die Experimente mittels RDE (rotierende Scheibenelektrode) werden für den Vergleich von supporteten Katalysatormaterialien verwendet, um die Polarisationsreaktivität zu bestimmen und miteinander zu vergleichen. Ursprünglich wurde ein existierendes Protokoll, das auf der Forschung an Protonenaustauschmembran-Brennstoffzellen (PEMFC) basiert, für die Tintenherstellung der siebbedruckten CLs verwendet. Durch ein modifiziertes Protokoll werden geeignete Trocknungsbedingungen, optimierte Ionomergehalte sowie eine vorteilhafte Auswahl von Dispersionslösungsmitteln für PEMWE Drucktinten erreicht.

Die Ergebnisse zeigen, dass die leistungsfähigste anodische CL einen Nafion®-Gehalt von 10 Gew.-% in der getrockneten CL hat, während für die Tintenrezeptur ein Massenverhältnis von 50:50 des Cyclohexanol-1,2-Propylenglykol-Gemisches verwendet wird. Dies führt aufgrund einer homogeneren Dispersion des trägerlosen Iridium black (Ir black) Katalysatorpulvers zu einem geringeren Innenwiderstand. Schließlich erzielen diese Verbesserungen ein Potential von 1,867 V @ 2 A/cm². Die getestete MEA weist dabei einen Ir-Gehalt von 1,88 mg/cm² innerhalb der anodischen CL auf. Dies wiederum führt zur Produktion von etwa 0,197 Standardlitern pro Minute (SLPM) Wasserstoff für jede Zelle mit einer aktiven Zellfläche von 10 cm².

List of Abbreviations

AC	alternating current	i.e.	id est
AST	accelerated stress test	IPA	isopropyl alcohol
ATO	antimony tin oxide	Ir	iridium
AWE	alkaline water electrolysis	IV	current-voltage
BET	Brunner-Emmet-Teller	kg	kilogram
BPP	bipolar plate	kN	kilonewton
BSE	back-scattered electron	MA	mass activity
CCE	catalyst coated electrode	MEA	membrane electrode assembly
CCM	catalyst coated membrane	NHE/SHE	normal/standard hydrogen electrode
C_{DL}	double-layer capacitance	O_2	oxygen
CHEP	cycloheptanol	OER	oxygen evolution reaction
CHEX	cyclohexanol	ORR	oxygen reduction reaction
CL	catalyst layer	PEM	proton exchange membrane
CV	cyclic voltammetry	PEMFC	proton exchange membrane fuel cell
DC	direct current	PEMWE	proton exchange membrane water electrolysis
DFT	density functional theory	PET	polyethylene terephthalate
DI	deionised	PG	propylene glycol / 1,2-propanediol
+e	electron	PGM	platinum group metal
e.g.	exempli gratia	Pt	platinum
ECSA	electrochemical active surface area	PTFE	polytetrafluoroethylene
EDX	x-ray spectroscopy	PTL	porous transfer layer
EIS	electrochemical impedance spectroscopy	PVP	polyvinylpyrrolidone
Eq.	equation	R	resistance
FEP	fluorinated ethylene propylene	RDE	rotating disk electrode
f	frequency	RHE	reversible hydrogen electrode
FIB	focused ion beam	rpm	rounds per min
(g)	gaseous	RRDE	rotating ring disk electrode
g	gram	SE	secondary electron
GC	glassy carbon	SEM	scanning electron microscopy
GDE	gas diffusion electrode	SLPM	standard litres per min
GDL	gas diffusion layer	TEM	transmission electron microscopy
GW	gigawatt	TNO	Netherlands Organisation for Applied Scientific Research
H_2	hydrogen	TPB	triple phase boundary
H_2O	water	WE	water electrolyser
HER	hydrogen evolution reaction	wt%	weight percent

1 Introduction

Hydrogen has the potential to become the principal energy carrier for an intended circular economy. Atomic hydrogen is the most abundant element (about 90% of all atoms in the universe), while H_2 fuel has the highest known energy content (122 MJ/kg) per mass amongst all known energy carriers [1]. Nevertheless, hydrogen is a secondary energy carrier as it is naturally bound to other elements and therefore has to be initially obtained from primary energy sources. These energy sources are plentiful and include renewables (e.g. solar, wind, hydro and biomass) as well as non-renewables (e.g. coal, gas and oil). Nowadays, almost all hydrogen (95%) is produced from fossil fuels and only 5% mainly from alkaline electrolysis (AE) [2]. Thereby, the conventional production of hydrogen consumes 6% of global natural gas and 2% of global coal output, while emitting 830 million tons of carbon dioxide per year [3]. Insofar, the transition to renewable and sustainable hydrogen production is inevitable in order to decarbonise the energy and fuel sector.

Overall, the achievement of sustainable hydrogen production will be a milestone on the way to an energy supply largely based on renewable energy sources. The electrical load peaks associated with intermittent renewables could be transformed into hydrogen by large scale electrolysis plants (GW-range), but the amount of the scarce iridium used for the anodic catalyst layer must be reduced while the operation lifetime has to be increased. The most beneficial production technique is electrochemical water electrolysis, which has the ability to store electrical energy from intermittent sources as fuel in chemical form for long-term in comparison to battery stacks. This enables higher amounts of renewables in the energy mix, while the electrolyser virtually has no harmful or toxic air pollution contribution.

An electrolysis cell is a device in which electrical energy is directly converted into chemical energy via an electrochemical redox reaction. Water electrolysers (WEs) only need water, electricity and heat to obtain hydrogen and oxygen as product gases. The most economic water splitting technique is currently low-temperature alkaline water electrolysis (AWE) due to the long operation time (90,000 h) and the usage of non-noble catalysts (e.g. Co, Cu or Ni) [4, 5]. However, the three major limitations of AWE are the limited partial load range, high ohmic losses across the length of the liquid electrolyte, which result in small current densities, and low obtainable operating pressures [6]. Whereas, the main advantages of proton exchange membrane water electrolysis (PEMWE) are the high-power density, quick start-up procedure,

good response to varying loads and the low operating temperatures. The heart of each PEM electrolyser is the membrane electrode assembly (MEA). MEAs consist of a polymer electrolyte membrane, a catalyst layer (CL) on both sides of the ionomer membrane and two porous transfer layers (PTLs) on the outside of the catalyst coated membrane (CCM). This 5-layer MEA is placed between two bipolar plates (BPPs), whereby the final components are the end plates to form a single cell, the so called 7-layer MEA. These cells can then be connected in series to create a cell stack, whereas the cells are connected via the BPPs and the initial and final cells are adjacent to the two end plates. Therefore, all MEA units are sandwiched in between the end plates.

The CL is the actual electrode of each electrolysis cell and must provide sufficient triple phase boundary (TPB) sites. These sites enable the three major transport processes namely electron connection to the PTL, proton conduction pathways to/from the membrane and water/gas exchange via the porous structure. The actual catalytic active material is only fully utilised if all three mechanisms are ensured by the immediate surrounding structure. Unsupported Ir or IrO_2 catalyst mixtures are still the standard active material in commercial PEMWEs [6]. In order to increase the area of the TPB, the usage of high-surface support materials (e.g. ATO, carbon black and TiO_2), improved MEA manufacturing techniques and the addition of an ionomer to extent the proton conductivity between both CLs are the three most viable optimisation operations. Whereby, increased surface areas lead to more activity of the catalyst and higher TPB densities. The ideal ionomer usage results in higher utilisation of the catalyst, reduced catalyst loadings and improved MEA performances. Therefore, the ionomer is an essential component to increase the performance by enabling higher current densities and prolonged operation time. These ionomer values are either measured in loadings (mg/cm^2) or weight ratios (wt%) of the ionomer in the CL.

The typical ionomer content values are in the range of 1 - 3 mg/cm^2 or 10 - 30 wt% respectively, to fill 35 - 50% of the porous void volume [7, 8, 9, 10, 11]. The typical active material for the rate-limiting anodic half-cell reaction is iridium or iridium/ruthenium mixtures, while the standard loading of iridium in commercial applications is 2 mg_{Ir}/cm^2 [12, 13]. Carbon supported platinum is the standard for the cathodic electrode and typical loadings are 0.5 mg_{Pt}/cm^2 in commercial applications. Current research efforts resulted in a reduction of the platinum loading at the cathode to 0.025 mg_{Pt}/cm^2 without significant performance impairment [14]. This means that the main challenge to achieve lower contents of platinum group metals (PGM) lies

in the anodic oxygen evolution reaction (OER). To obtain competitive cost factors in comparison to AE and therefore ensure wide application potential despite the limited resource capacity, the loading of iridium has to be lowered to preferable 0.5 mg_{Ir}/cm^2 for the next generation of PEMWEs. Loading values of unsupported Ir catalysts below 0.5 mg_{Ir}/cm^2 would result in inhomogeneous surface coverage and subsequently reduced performance values [14]. In addition to the catalyst reduction, the current density has to be kept as high as possible, while an increase in the obtained voltage should be limited to sustain a high operation efficiency. The challenges associated with this trade-off form the basis of this research project.

This study seeks to investigate the optimal ionomer loading for the anodic CL. The research focus lies onto the MEA preparation via screen-printing and the related catalyst ink composition optimisation. The ionomer content is adjusted accordingly for unsupported Ir black catalysts. Beyond that three dispersion solvent mixtures have been utilised to manufacture the anodic CLs. Therefore, the drying conditions have been aligned with the varying catalyst ink composition. The activity and stability of the obtained MEAs are verified with IV polarisation curves and electrochemical impedance spectroscopy (EIS). Furthermore, cyclic voltammetry (CV) studies are realised with a rotating disk electrode (RDE) to obtain the activity of Ir containing catalyst supports, namely TiB_2, TiO_2 and ATO. The results have been compared to a commercial TiO_2 supported Ir solution. The overall target remains to increase and/or sustain the performance of the CL, while reducing the iridium loading to make PEMWEs more competitive for the wide-spread application of a sustainable hydrogen economy.

In the following chapter, the theory and the fundamental equations relevant for PEMWEs are explained in more detail. In chapters three and four, the experimental set-up and the results obtained are discussed before a summary of the main findings and a brief research outlook are given.

2 Methods and Fundamentals

The crucial properties of PEMWE systems are its performance, durability and cost efficiency. Therefore, the fundamental background of electrochemical, mass transport and material phenomena have to be revealed to gain knowledge about the essential deterioration processes in order to reach the required operation targets. The focus lies on the CCM, as this is the crucial component of each MEA and the preparation and homogeneity of this component are decisive for the overall performance. Therefore, the correct manufacturing of CCMs is of great importance, whereas the common pathway for the catalyst containing ink preparation involves magnetic stirring, ball-milling and ultrasound treatment. The application onto the membrane is done by screen-printing, doctor blade coating, spraying and/or decal transfer. Moreover, influences on and from the individual parameters have to be measured and determined separately in order to be able to draw consistent conclusions about the extent to which the component is affecting the overall performance and how the cell design must be altered. For this purpose, numerous non-destructive, in-situ and ex-situ measuring methods are used, which are presented in this chapter after initially explaining the working principle of PEMWEs.

2.1 Working principle of PEMWE

The 5-layer MEA structure of a typical PEMWE is depicted in Figure 2-1 (see next page). The inlet for the preheated liquid water is on the side of the anodic bipolar plate (BPP) and the water is pumped through the flow channels into the PTL, while product gases are removed from the cell. The water reaches through mesoporous pathways the active sites of the anodic CL, where the water molecules are oxidised. The resulting protons (H^+) are transported with accompanying water molecules through the electrolyte membrane into the cathodic CL. The oxygen is transported in counterflow manner back to the BPP on the anode side and removed from the cell. Although, there happens to be an additional crossover water stream and a smaller back-diffusion hydrogen flow from the cathode to the anode. The released electrons are transferred within an external bypass to the cathode and recombined with the protons at the cathodic active sites to form hydrogen. The hydrogen gas is then transported through the cathodic PTL to the BPP, where it is removed and dried to obtain pure hydrogen (99.99%).
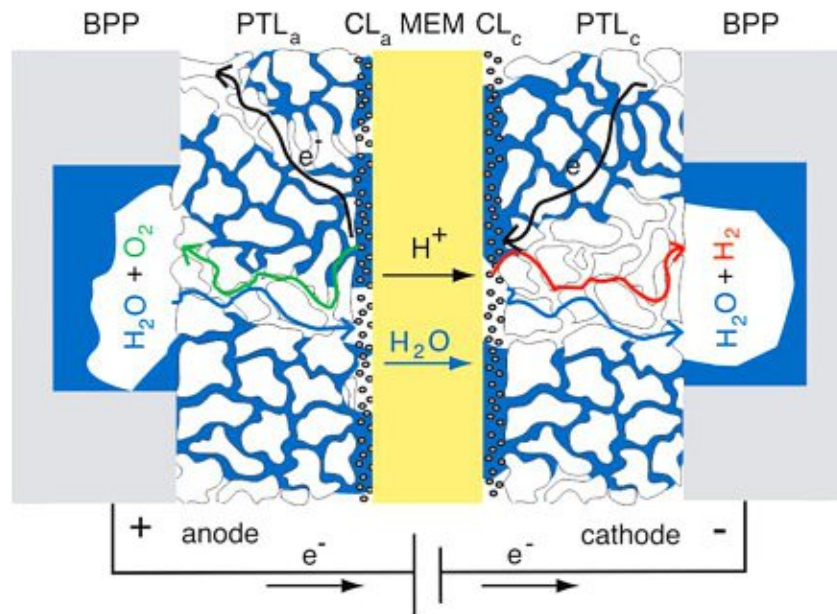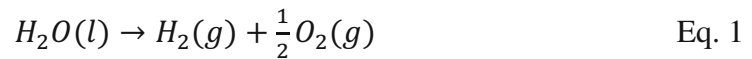
Figure 2-1: Schematic structure of PEMWEs [15]: The central polymer membrane (yellow) is coated with the anodic and cathodic CL. The 3-layer CCM is enclosed on either side by the PTL and BPP. Moreover, the electron transfer, proton transport and mass flow (water, hydrogen and oxygen) mechanisms are included in the illustration.

The overall endergonic water splitting reaction is the combination of the anodic and the cathodic half-cell reactions (OER and HER) of the acidic electrolyte cell, given in Eqs. 1 - 3.

$$H_2O(l) \rightarrow H_2(g) + \frac{1}{2}O_2(g) \qquad \text{Eq. 1}$$

$$H_2O \rightarrow 2H^+ + \frac{1}{2}O_2 + 2e^- \qquad \text{Eq. 2}$$

$$2H^+ + 2e^- \rightarrow H_2 \qquad \text{Eq. 3}$$

The electrochemical water splitting reaction has a standard free reaction energy of ΔG_0 = 237 kJ/mol at standard conditions of 25 °C and 1 bar and a theoretical cell potential of E_0 = 1.23 V. This cell potential is equal to the reversible anode potential compared to the standard hydrogen electrode (SHE) as the reversible cathode potential is zero. Most PEMWEs operate at temperatures of 80 °C as elevated temperatures are beneficial for faster kinetics and therefore reduce the anodic activation overvoltage [16]. Nevertheless, the operation temperature has to be kept below 100 °C since the polymer membrane and the ionomer in the CL are negatively affected by a temperature increase and characterised by reduced conductivities. This process already has a growing, influential affect at operation temperatures of 80 °C without proper humidification and is even more pronounced at higher temperatures [7].

The thermodynamic efficiency η of water electrolysers in Eq. 6 is the ratio between the Gibbs free energy ΔG in Eq. 4 respectively Eq. 5 and the enthalpy ΔH.

$$\Delta G = \Delta H - T\Delta S \qquad \text{Eq. 4}$$

$$\Delta G = -R\,T\,ln(K) = -n\,F\,E_{we} \qquad \text{Eq. 5}$$

$$\eta_{WE} = \frac{\Delta H^T}{n\,F\,E_{WE}} \qquad \text{Eq. 6}$$

The amount of the transferred electrons is given by n and there are two electrons transferred in the water splitting reaction, while F is the Faraday's number (F = 96,487 C/mol). The high heating value of hydrogen at 80 °C (ΔH_{80} = -284.04 kJ/mol) combined with a typical operational current density of 1 A/cm^2 and a corresponding voltage of E_{WE} = 1.6 V gives the high efficiency value of η_{WE} = 91.99 % for the electrochemical PEM water electrolyser reaction [17]. When the loading of the iridium is reduced to 0.5 mg/cm^2 and the ratio of the current density and potential remains the same, the specific power density is 3.34 kW/g$_{Ir}$.

The theoretical cell potential at standard conditions and the equilibrium potential at actual operation conditions can be described by the Nernst equation in Eq. 7. This equation describes the change of the Gibbs free energy during water electrolysis operation.

$$\Delta G = \Delta G_o + R\,T\,ln\left(\frac{p_{H2}\,p_{O2}{}^{0.5}}{p_{H2O}}\right) \qquad \text{Eq. 7}$$

2.2 MEA fabrication

The fabrication method of the MEA has to be chosen wisely to obtain high scalability, reproducibility and low time expenditure, while matching with the requirements and properties of the catalyst itself. To ensure homogeneous distribution and achieve a mesoporous morphology, the calcined sample is normally processed with a ball mill, whereas the ink solution is thoroughly dispersed within an ultrasonic bath. This ink is then applied via the screen-printing method onto a decal material. This coated decal is then transferred and hot-pressed onto the polymeric Nafion® membrane to obtain the CCM. The addition of the PTL and subsequent assembly results in a 5-layer MEA design, which is then mounted between the BPPs to form an electrolyser stack. The individual production steps are described in more detail in the following sections.

2.2.1 Screen printing

This application method uses a moving squeegee to press the catalyst ink from the screen sieve onto the underlying substrate [18]. Screen printing is a special kind of doctor blade coating with the main characteristic that a patterned screen is used as the application mask. Here the void volume is controlled by the mesh count and this later designates the amount of ink that is applied onto the substrate material. The screen or mesh is fixed on a frame and the suitable amount of ink is spread onto this screen, where the preferred printing scheme is left amenable while the remaining undesired area is masked out. Hereby, the screen defines the quality of the seal and is optimally used for flat surface printing [19]. It should be noted that the gap size of the perforated screen has to be larger than the catalyst particle to avoid clogging as this would result in an inhomogeneous distribution of the ink. A drying step follows after each print when the ink has been pushed through the mesh and the decal is removed from the screen printer. Thereby, the dispersion solvent is removed and the transferred catalyst material fixated onto the underlying substrate. This procedure is repeated until the complete ink is transferred or the targeted catalyst thickness is achieved. This schematic screen printing process is depicted in Figure 2-2.
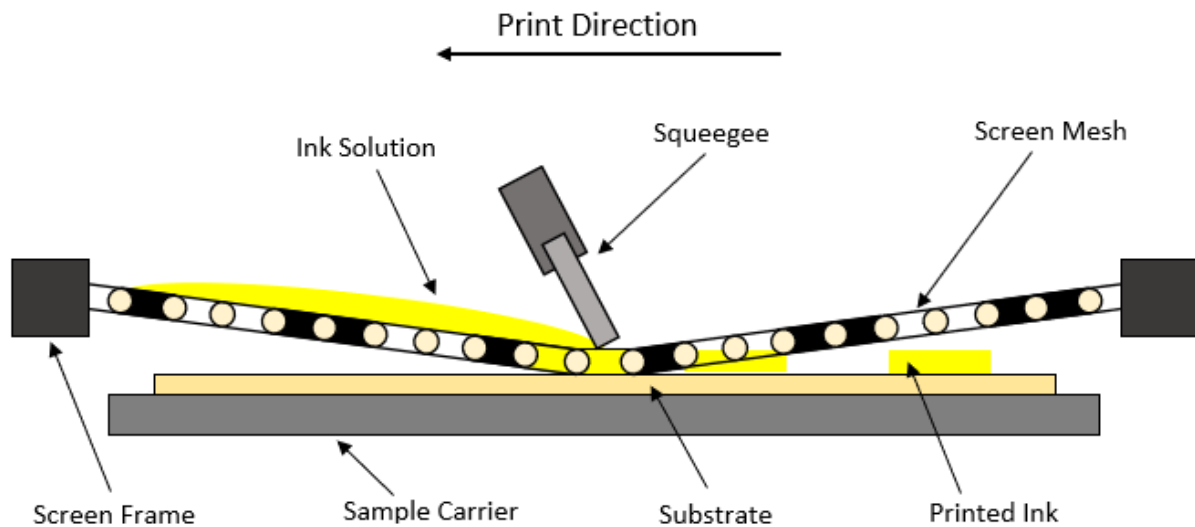

Figure 2-2: Schematic of the screen printing method based on Kumari et al. [20], which was modified and applied to MEA fabrication.

Major deposition parameters such as the pressure applied to the squeegee, the snap-off distance (i.e. distance between the squeegee and the desired substrate surface), the operation speed of the squeegee upon activation and the ink's viscosity are influencing the effectiveness of the application [19]. At a certain pressure on the squeegee, the mesh is completely filled with the ink and further increased pressure will not lead to improved print qualities. In general, lower printing speeds are beneficial for high viscous inks, whereas high printing speeds are

advantageous for thin ink solutions [21]. In any case, the ink has to be more viscous to prevent leakages across the porous substrate. This means that inks for screen printing have lower solvent ratios and a higher ionomer content in comparison to spraying techniques. Additional to the viscosity, the change under mechanical shear stress is influencing the flow properties and has to match with the mesh requirements and the rheology of the ink. The shear rates during screen printing can range from 0 - 1000 s^{-1}, while a typical print operates at maximum shear rates of 300 s^{-1} [21]. M. Hill found for well dispersed catalyst inks (Pt/C in 3/0.5 ml of 1,2-propanediol/isopropanol) the optimal screen printing conditions to be 3.4 bar with a squeegee angle of 22° and a printing speed of 0.6 m/s [21].

The screen printing method is usually used for an indirect application due to the fact that the ink is mostly applied onto a blank decal sheet before it is transferred via hot-pressing onto the polymer membrane. Direct application is also possible, but requires that the membrane has already been converted to the Na$^+$ form to stabilise the CL and to avoid potential crack formation. This direct application can lead to pronounced swelling and has to be taken into account for the selection of the dispersion solvents [22]. In general, screen printing is an optimal technique with regard to printing time and reproducibility. It can be fully automated with the inclusion of a continuous heating oven for series production. In addition, the high material throughput, homogeneity and positional accuracy (shape and thickness) are further features to ensure cost effectiveness and both high quality and quantity requirements for the industrial application [19].

2.2.2 Decal transfer

The decal transfer is the most common method used in PEMWE research. In contrast to direct screen printing or doctor blade coating, the catalyst is applied in solid form rather than in liquid form onto the membrane. A challenge for decal transfer methods is to ensure that the complete catalyst transfer is obtained without significant residual catalyst material remaining on the decal sheet. The main advantage is that possible problems of the direct application methods such as swelling induced crack formation and inhomogeneous distribution are avoided, if the membrane is correctly pre-treated. The membrane has to be converted into the Na$^+$ form to avoid swelling during the decal transfer induced by the high hot-pressing temperatures [23].

First of all, the sheet has to be properly cleaned and dried before the ink is spread onto the decal to form the CL. During the fabrication, the ink solution (i.e. supported catalyst, ionomer and dispersion solvent) is applied through brushing, painting, spraying or coating onto the PTFE

sheet [6]. The CL is prefabricated on this PTFE sheet, dried and subsequently hot-pressed onto the pre-treated membrane. The pressure range is 0.1 - 4 MPa and the temperature is typically kept between 120 - 190 °C. The decal materials are removed after being hot-pressed and subsequently cooled. The decal sheet is usually weighed before and after the hot-pressing step to determine the catalyst material loss and to calculate the resulting loading of the CL.

2.2.3 Ultrasonic bath

A sound wave must have a frequency of above 16 kHz and below 500 MHz to fall into the ultrasound range. This definition is valid for liquid and solid media [24]. Whereby, the low frequency ultrasound (20 - 100 kHz) is usually used for ultrasonic cleaning baths [25]. This ultrasonic bath method is used for all kinds of cleaning purposes such as the cleaning of the ring disk electrode (RDE). Additionally, it is used for the dispersion and homogenisation of the catalyst ink in almost 90% of all catalyst ink preparations of low temperature fuel cell research prior to the fabrication of the CCMs [25]. The adjusted ultrasonic parameters such as frequency, power and duration affect the final ink composition, morphology and structure. Whereby the influence of the water temperature onto the cell's performance is negligible. Thus, a temperature control is not required for this method. In general, the used solvent influences the effect of the ultrasonic cavitation mechanisms, e.g. IPA lowers these effects [26].

An effective dispersion of the ink is key to obtain homogeneous CL/electrodes with improved electrocatalytic activity for the OER, HER and ORR. ECSA and RDE tests are used to show the effects of the ink dispersion and to find the optimal preparation conditions for each ink composition. Both energy and duration of the ultrasonic treatment have a significant effect onto the reproducibility and degradation mechanisms [27]. Shorter ultrasonication times (< 15 min) result in inhomogeneous samples, whereas long ultrasound exposure times (> 100 min) lead to increasing losses of the ECSA. Medium ultrasonic powers of 2 - 5 W (i.e. 20 kHz) are better suited and result in beneficial catalyst structures [28]. Especially the Nafion® solution can be affected by polymerisation or even depolymerisation processes. These processes are caused by radical coupling and cavitation, which lead to a viscosity increase or decrease when inappropriate conditions are applied. It was found that between 15 - 30 min of ultrasonication time is ideal to produce homogeneous catalyst dispersions, which usually lead then to reproducible test results [25, 26].

2.2.4 Ball milling

The high energy ball milling technique is used to produce alloys and composites with a nanocrystalline structure. The moving balls apply their kinetic energy to the catalyst material and thereby break chemical bonding, decrease the particle size, change the particle shape and produce more surface area [29]. The collisional and frictional forces of the tumbling milling balls break down catalyst agglomerates, which can be obtained after the calcination treatment. Zirconia balls are usually used due to their high hardness and fracture toughness compared to the catalyst material. Major operation parameters are both the rotational speed and the milling time. The long operation time is the main disadvantage of this milling device as smaller particles get increasingly difficult to disaggregate. The behaviour of the zirconia balls in dependence of the rotational speed is shown in Figure 2-3 for a horizontal ball mill.
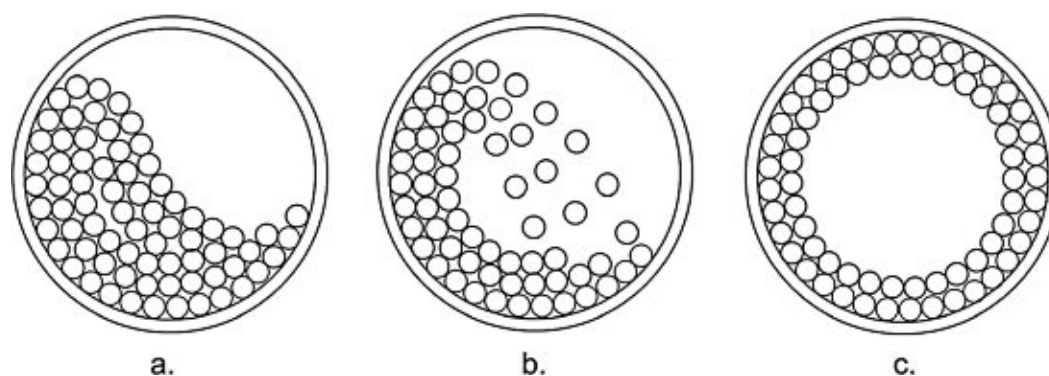

Figure 2-3: The rotational speed is increased in the direction of a to c [30]. The grinding process has the highest efficiency in configuration b due to the maximization of the gravitational force.

Both size and shape of the milling media are important physical dimensions as well as the remaining void volume and the ratio of the milling media to the catalyst powder. On the one hand, a reduced size of the milling media guarantees that a higher amount can be used, which increases the probability of contact impact. On the other hand, the smaller mass of the zirconia balls has less impact energy for the separation of the ground material agglomerates. An advanced planetary ball milling device generates shear and impact forces. Therefore, these devices are even suitable for the premixing of high viscous inks for screen printing, while reducing the operation times compared to simple ball milling devices. All in all, high energy ball milling assumes a vital role in the synthesis of catalysts, increasing the interfacial surface area of substrate and catalyst material while promoting the proper distribution of the catalyst.

2.3 Electrochemical setup and methods

Various analytical techniques can be used to characterise the catalyst ink and monitor the MEA performance. The electrochemical techniques and devices, which have been used in this report,

are discussed briefly in this section. In general, the validation of catalysts requires quick and reliable screening methods to assess the performance potential in an early stage of development, to preselect promising configurations and compositions as well as to obtain results in an efficient manner.

2.3.1 CCM and cell setup

The central component of each PEMWE is the Nafion® membrane, which separates both half-cell redox-reactions and limits the hydrogen exchange rate. This ionomer membrane is coated on both sides with the CL, i.e. the actual active material for the reaction. On one side is the iridium containing anodic layer and on the other side is the platinum containing cathodic layer. The PTL is made from carbon black with a high-surface area as the support material for the cathode side and sintered porous titanium foil is used for the more corrosive prone side of the anode. The BPPs are both manufactured out of platinum-coated titanium, which functions as the contact material. Thus, this layer provides the structure for the flow field of the cell. Each of these layers contributes a certain resistance due to the dimensional extent of the layer. The electrode/electrolyte interface has an additional specific phase element, whereas each respective electrode has a unique diffusion impedance influence onto the cell performance [31]. Overall, exactly four electrons have to be exchanged in the PEMWE water splitting reaction to obtain molecular oxygen at the anode, which results in two hydrogen molecules at the cathode, whereas the exact reaction steps are still subject to debate [31].

2.3.2 Polarisation curve

The polarisation curves are used to determine the exact OER kinetics and mass transfer resistance under similar operation conditions as in the actual PEMWE application. Due to its simplicity, it serves as a standard characterisation method for fundamental performance evaluation of electrochemical cells, while it is operated under a set of constant parameters [32]. Measurements can be obtained in galvanostatic or potentiostatic manner. The data chart is obtained when the cell potential is plotted as a function of the current density, whereas high current densities at low voltage values are intended for productive water electrolysis. The characteristic voltage sweep of the polarisation curve increases with rising power/current densities. This effect can be seen in Figure 2-4 (see next page).
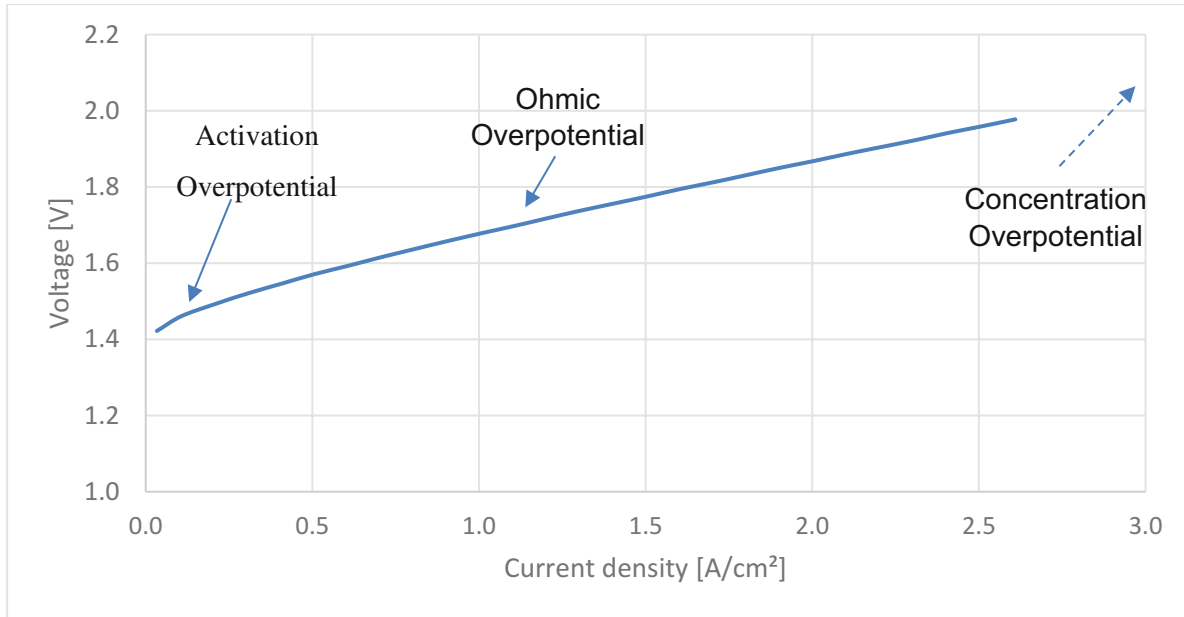
Figure 2-4: Typical PEM electrolyser polarisation curve obtained in this study.

The typical rising curve consists of three distinct stages and is based on the Butler-Volmer kinetics. The first stage represents the activation polarisation, the intermediate, linear stage is the ohmic polarisation due to component resistances and the third and last stage forms the concentration/mass transport polarisation [33, 34]. If the obtained potential values are multiplied by the corresponding current density and in turn plotted, then the obtained chart depicts the correlation between the power density versus the current density [32]. Moreover, the first order deviation of the polarisation curve leads to the differential cell resistance [31].

The activation polarisation is mainly influenced by the catalyst and the structure of the CL, while the concentration polarisation is caused by mass transfer restrictions. The difference between the non-equilibrium operating potential E and the equilibrium reversible potential E_r gives the value of the overpotential, which is required to maintain the reaction. The correlation between these two potentials is given by the Butler-Volmer equation. Thus, the Butler-Volmer equation in Eq. 8 can be used to describe the current density for non-equilibrium operation.

$$j = j_0 \left\{ exp\left[\frac{-\alpha_{ox} \, z \, F \, (E-E_r)}{R \, T} \right] - exp\left[\frac{\alpha_{red} \, z \, F \, (E-E_r)}{R \, T} \right] \right\} \qquad \text{Eq. 8}$$

The actual cell potential is required to sustain the electrolysis reaction. It can be calculated according to Eq. 9 with the reversible voltage term E_r and the contributions of activation, ohmic and mass transfer losses.

$$E_{cell} = E_r + E_a + E_o + E_m = E_r + IR_a + IR_o + IR_m \qquad \text{Eq. 9}$$

The prevailing activation losses are characterised by the reaction kinetics and can be calculated using the Tafel equation (see Eq. 10), which is obtained from the linearisation of the Butler-Volmer equation.

$$E_a = 2.3 \frac{R\,T}{z\,F} \left[log(j_0) - log(\text{j}) \right] = b \log \left(\frac{j_o}{j} \right) \qquad \text{Eq. 10}$$

Consequently, the polarisation curve can be utilised for the determination of the influence of varied operation conditions (e.g. T, P, V and flow rate) and dimension parameters (e.g. thickness, composition, structure and additives) onto the overall performance. However, this method is not suitable to distinguish between the influences from individual components or mechanisms and cannot be applied during the actual electrolysis application, which makes the measurement method quite time-consuming. Overall, the polarisation curve method enables a simple comparison of different catalyst materials in the pre-selection process.

2.3.3 Cyclic voltammetry

This method is a valuable in-situ technique, especially for determining the electrochemical active surface area (ECSA) within the catalyst layers and the corresponding double layer capacitance C_{DL}. Hereby, the current is measured while the potential is switched over recurrently with linear time steps between two defined voltage limits [32]. This linear potential scanning rate is normally in a range of 1 - 1,000 mV/s [35]. The cyclic voltammogram is obtained by expressing the current over the voltage. The resulting current shows a peak at each point when an active electrochemical potential is realised and stabilises once more after the available reactants have been consumed [32]. Therefore, the relative reaction rate or diffusion proceedings are assessable by the cyclic voltammetry (CV) [36]. Attention must be paid in particular to the fact that artefacts can be present, which is resolved by adjusting the purge flow (e.g. nitrogen or argon). Several initial cycling steps are realised to remove potential surface contaminants before the CV is recorded. From the data of the CV the ECSA can be easily measured, which is an important indicator for the CL´s activity.

2.3.4 Linear sweep voltammetry

This irreversible analysis method, which is similar to the CV and also applies an inert gas stream, is used to measure inefficiencies due to the hydrogen gas crossover [32]. The current increases with rising potential as it is generated solely through the hydrogen crossover. The hydrogen crossover is altered by the operation parameters and membrane degradation [32]. The linear sweep method is realised through the control of the potential, whereas the incurred current is measured. Then the current density is plotted against the potential and either a

constant or a linearly ascending curve with increasing electrode potential is obtained. Increasing values of the current are due to the resistance caused by internal shorting [37]. This resistance is then calculated based on the curve´s slope in the obtained chart.

Now that the methods for the pre-characterisation and pre-selection of promising test samples and compositions have been described, the following chapter describes the most important tool for determining the actual performance of MEAs used in hydrogen-generating PEMWEs.

2.4 Electrochemical impedance spectroscopy

This is the primary non-invasive and non-destructive diagnostic tool for the in-situ characterisation of MEAs used in both stacks or single-cell experiments of PEM fuel cells and water electrolysers. The method is based on the linear response theory, which implies that the system response to an interfering signal is linear [37]. The aim of this fast response method is to determine the individual contributions of each component. It is mainly used to measure the protonic conductivity. Moreover, thereby implemented accelerated stress tests (ASTs) are crucial for the understanding of encountered degradation mechanisms under realistic or simulated operation conditions. Electrochemical impedance spectroscopy (EIS) measurements are preferentially performed in the frequency range of 0.1 - 10,000 Hz by a four-electrode measurement configuration consisting of a working electrode, a counter electrode and two reference electrodes [38]. The functional principle is based on the fact that in addition to the operational direct current (DC), a perturbation alternating current (AC) sine with known amplitude and frequency is applied. This perturbation AC is varied in the galvanostatic operation mode through frequency adjustments, while the obtained cell voltage response signal including amplitude and phase is measured. Whereas, in the potentiostatic operation mode, the voltage is applied and the AC response is measured [38]. The AC induced impedance Z is calculated as the ratio of the voltage divided by the current in galvanostatic mode (see Eq. 11). The inverse of this value would be used for the potentiostatic operation mode.

$$Z(f) = \frac{U_{AC}(f)}{I_{AC}(f)} = |Z(f)| * e^{i\,\theta(f)} \qquad \text{Eq. 11}$$

This dynamic operation enables the observation of time-dependant degradation processes within the cell through the available broad range of applied frequencies. The range of the perturbation frequency is between 0.01 Hz and 10^6 Hz [38]. Therefore, they are used to evaluate and optimise electrochemical and transport processes of diverse MEA configurations. These processes include the double layer charging, charge transfer, interfacial capacitance as well as

gas and water diffusion [38]. Additionally, EIS is used in PEMWEs to characterise and optimise the structure and homogeneity of the MEA, to quantify modifications of the components and to visualise effects from changes of the operation parameters [38]. Furthermore, non-linear least square analysis is used for the observed spectra to obtain values and draw conclusions about the electrochemical parameters. The exact methodical settings and procedure steps for a validated EIS measurement are given in the guideline written by Malkow et al. [38].

The graphical representation of the analysis is the Nyquist chart, which is obtained by plotting the negative imaginary impedance Z" against the real part of the impedance Z'. It should be noted that high frequencies are located further left on the x-coordinate. Once again, the plot can be divided into the areas dominated by activation, ohmic and mass transfer losses (see chapter 2.3.2). The responsible voltage losses result from charge transfer activation, the ion and electron transfer as well as the water/oxygen exchange transfer. Nevertheless, the correct interpretation or allocation is complex and it is still a debated endeavour [32]. Another plot from EIS data is the Bode chart, which additionally contains information about the phase shift ϕ but is of minor usage as it is less sensitive to changes. Thus, the Nyquist plot is preferentially used. An exemplary Nyquist plot is portrayed in Figure 2-5, whereas the mass transfer resistance is pronounced. In real test simulations, however, this arc is not as pronounced.
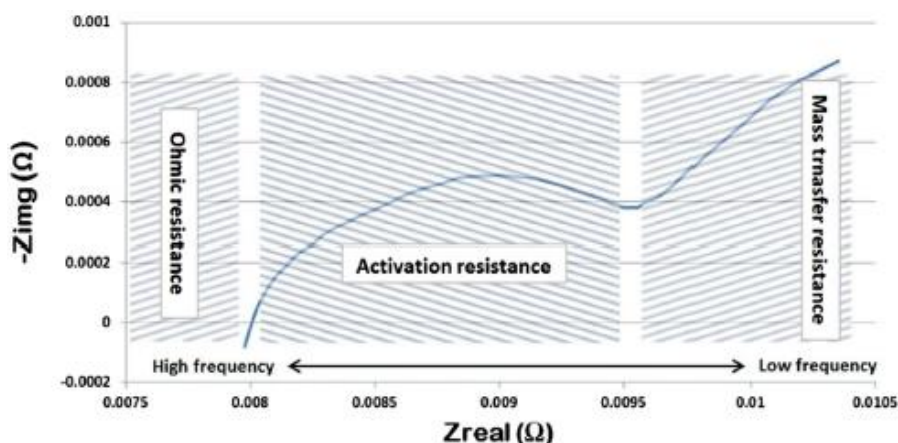

Figure 2-5: Typical Nyquist plot with the three characteristic resistance induced domains for a single PEMWE cell [34].

In the Nyquist chart the activation resistance is represented by the semicircle, while the internal ohmic resistance loss is obtainable at the high frequency interception with the abscissa axis [32]. The activation losses are mainly due to the OER charge transfer kinetics at the interfaces between the CL and the neighbouring layers [31, 38]. Whereby, smaller semicircles in the graph define accelerated reaction kinetics [34]. Furthermore, the value of the ohmic

resistance includes all components and interlayer contact resistances, whereas the membrane resistance is mainly responsible for the occurring losses. Thus, the thickness of the ionomer membrane is decisive for the ohmic resistance and must be taken into account when a comparison with other data sources is taken. The mass transfer effects are portrayed at low frequencies through a second semicircle (i.e. finite diffusion) or a 45° line (i.e. infinite diffusion) and are due to the sluggish oxygen/water exchange [34]. In general, the measured resistance of the anode is much larger than the cathode and therefore usually only one semi-circle is observed.

These Nyquist plots are obtained from MEA testing used in PEMWEs for the accurate examination under real life test conditions. The MEA characterisation is determined using the EIS method. An advantage of the quicker RDE method is that only small quantities of the catalyst ink mixture are necessary, therefore it can be used to preselect promising catalyst candidates for the MEA fabrication.

2.5 Rotating disk electrode

This technique is used for the initial performance evaluation since only small catalyst amounts are needed to obtain an activity assessment of the catalyst specimen. The intrinsic stability is only accessible to a limited extent as the observed degradation and rising potential lead to apparent stability values. The measured values are the result of a partial shielding of the active sites by oxygen bubble formation [39]. Therefore, the lifetime durability has to be verified under practical operation conditions within the MEA application. The electrochemical cell used for the RDE device works according to the three-electrode principle, namely the working, counter and reference electrode. The normal hydrogen electrode (NHE) or the reversible hydrogen electrode (RHE) can be used as a reference electrode. The current flows between the counter and working electrode, while the reference electrode enables an exact measurement of the applied potential [40]. The planar disk of the working electrode is located within a ring of inert material and is either made out of glassy carbon (GC), graphite carbon or noble metals such as Pt or Au [41]. The golden working electrode is especially corrosion-resistant and functions as the current collector on which the catalyst sample is coated for the electrochemical stability tests. The electrode's shaft is associated with the motor and a control box to achieve high rotation rates per minute (rpm). This rotation is usually between 100 - 10,000 rpm to avoid long operation times and to obtain turbulent flow characteristics [41].

The RDE has to be located in the middle of a large volume electrolyte cylinder to gain an optimal flow field [41]. The used electrolyte is 0.5 M H_2SO_4 to achieve a 1.0 M H^+ aqueous solution. The gas inlet and outlets are used for the purge gas (i.e. argon and nitrogen). Optionally, additional inlet and outlets are used for heating or cooling liquids to control the temperature. An advanced version of the RDE is the rotating ring disk electrode (RRDE), which is used to study multi-electrons processes, the kinetics of slow electron transfers, adsorption/desorption steps as well as electrochemical reactions. Thus, the fundamental properties of electrocatalysts are accurately obtained in a faster manner than with the RDE.

The application method has to be strictly followed to achieve repeatable and comparable results. Before the ink solution is applied onto the surface of the RDE, the disk has to be polished with γ-Al_2O_3 in order to obtain a smooth surface. Successive, repeated washing with deionised water (DI water) follows and the ultrasonication of the components represents the next step to remove any adsorbed residues. Subsequently, the ink solution containing the catalyst is pipetted onto the mirroring surface of the RDE tip and dried until the solvents are removed and the surface is coated with a homogeneous catalyst layer. The loadings of the ionomer and catalyst can be calculated with the ink volume, the ink's composition and the electrode surface area. The cylinder is flushed with inert gas to discharge any solute gases. Then, the assembled working electrode is inserted into the electrochemical cell for the actual measurement. The electrolyte filled gap between the working electrode and the reference electrode causes a measurement error due to the electrolyte resistance R, which has to be compensated for in the calculation. This encountered iR drop of the solution is minimised by placing the catalyst-coated working electrode close to the reference electrode but far enough to avoid any blockage of the solution flow [41]. Moreover, the obtained current density is predominantly controlled by the electron transfer kinetics. The ionic transfer is influenced by the diffusion and convection, if there is no encountered convection within the testing apparatus the ionic transfer is determined by the diffusion processes. This results in a prolonged mechanism's reaction when the thickness of the diffusion layer is increased [41]. Techniques to measure the ionic resistance of the CL have been reviewed by Karan [42]. Moreover, the RDE includes stirring as well as electrode rotation to ensure a steady-state operation mode. Fick's second law can then be used for the calculation of the reactant concentration change.

2.6 BET surface area of porous materials

This widely used method measures the specific surface area, pore size and pore volume distribution. Nitrogen or argon adsorption/desorption isotherms are used to calculate the

specific surface on the basis of the Brunner-Emmet-Teller (BET) equation. The detailed isotherm type limitations and specific terms of the BET application are given by Thommes et al. [43]. However, the advanced density functional theory (DFT) is more useful than the BET equation for the size distribution of nanoporous materials because of the substantial contribution of nanopores. The surface value obtained by the BET method depends on the operation temperature and the location method of the pressure range [43]. Both volumetric and continuous flow measurements are used to obtain the amount of gas adsorbed onto the solid surface. The BET equation is given in Eq. 12 (see below). In the BET equation n is the specific amount of gaseous adsorbent, which is adsorbed at the relative pressure ratio p/p_0, and n_m is the specific monolayer capacity. C describes the shape of the isotherm, respectively the type of the hysteresis curve and is calculated as C = 1 + slope/intercept of the linear plot.

$$\frac{\frac{p}{p_0}}{n\left(1-\frac{p}{p_0}\right)} = \left(\frac{C-1}{n_m C}\right)\frac{p}{p_0} + \frac{1}{n_m C} \qquad \text{Eq. 12}$$

The BET area is then calculated from the derived monolayer capacity according to the following equation Eq. 13, where a_s(BET) is the specific area of the sample, N_A the Avogadro's number, σ_m the molecular cross-sectional area with the value of $\sigma_m(N_2) = 0.162$ nm^2 for nitrogen and m is the mass of the adsorbent.

$$a_S(BET) = \frac{n_m\,N_A\,\sigma_m}{m} \qquad \text{Eq. 13}$$

The measurement procedure is as follows. First, the sample has to be properly outgassed by vacuum or non-reactive purge gas to remove all adsorbed gases and vapours from the surface. The physical adsorption is made possible by the weak van-der-Waals forces between the adsorbate molecules and the adsorbent surface area. The ECSA is largely dependent on the morphology, which in turn depends on the preparation method of the catalyst. When the adsorbate gas is nitrogen, p/p_0 values of 0.10, 0.20, and 0.30 are sufficient for the three-point measurement method. In general, smaller crystallites have a larger, summarised surface area due to a larger number of surface molecules. Ir black and IrO$_2$ samples have a typical BET surface area of 18 m^2/g and 112.8 m^2/g respectively [23, 44].

After the description of various physical and electrical analysis methods, the following section is devoted to a comparison between the SEM and TEM imaging methods, which are used to achieve a closer, optical examination of the sample's structure and its layer´s thickness.

2.7 Electron microscopy

The morphological and compositional properties of the MEA are measured by scanning electron microscopy (SEM) and transmission electron microscopy (TEM) methods. Both methods are used for the characterisation of the CL's physicochemical properties. However, SEM is typically used for the analysis of agglomerate and grain size as well as pore size distribution, while TEM is more suitable for the analysis of Ir particle sizes, shapes and the ionomer distribution. The SEM analysis is much faster and has fewer restrictions than the TEM imaging. However, TEM techniques provide more details on internal structures and the near-atomic resolution after a suitable preparation of the sample. Thus, the combination of both methods enables the investigation of the catalyst's distribution on and within the support material of the CL. A comparison between those two methods follows to explain their respective functionalities in more detail.

2.7.1 Scanning electron microscopy

The high-vacuum, ex-situ SEM method uses a cathode to produce the high energy electron beam for the examination of the sample's surface and cross-section. The cross-sectoral analysis is very useful for degradation studies, involving pictures before and after the electrolysis process, which is used for elemental mapping in low-loaded MEAs [45]. SEM devices apply an electron beam with a wavelength of 0.12 Angstroms, which results in magnifications of up to 10,000 [21]. The function principle is based on the fact that the electrons are bended and accelerated by several electromagnetic lenses into the keV range to obtain a high magnification resolution and enable periodically scanning of nanometric areas. Thus, the degree of homogeneity of the surface is ascertainable, which is used to detect unfavourable ionomer patches on the surface and the proper distribution of the ionomer in macropores. This allows a comparison of the influence that different ink solvents have on homogeneity and thus on the MEA performance [46].

The simultaneous detection of primary beam induced secondary electrons (SE) and back-scattered electrons (BSE) allows to obtain morphological information and the material's composition altogether [47]. High numbers of SE result from larger angles of incidence, which becomes visible as steep edges appear brighter in the SEM images. The images from BSE are brighter for heavy elements since they backscatter more electrons. The mass ratio and atomic ratios of the catalyst and support material are determined with the usage of energy dispersive x-ray spectroscopy (EDX) for the µm depth range of the probe. SE are essential for analysing the first tenths of the nm area of the subsurface, while BSE are used for the deeper layers in the

100 - 1,000 nm range. SEM devices are used to attain high resolution images, quantitative elemental analysis and fast elemental mapping. In combination with focused ion beam (FIB) the 3-dimensional reconstruction of the CL is possible, which is based on a series of consecutive 2-dimensional images.

2.7.2 Transmission electron microscopy

The TEM method is used to analyse the microstructural morphology and the catalyst dispersion within thin specimen of the CL. For instance, the shell thickness of inverse-opal electrodes can be measured [4]. Moreover, additional information about the particle sizes and agglomeration state of the catalyst can be obtained. The specimen preparation is an important aspect of this technique as only thin specimen are fully mappable and enable the creation of micrographs under minimum energy losses. The function principle relies on a high energy beam of electrons, which is shone through the thin specimen. The beam is generated with an electron gun and this generated beam is subsequently focused by condenser lenses. The transmitted beam is refocused by the objective lens to create an image and this image is further enlarged by intermediate and projector lenses. Light areas represent locations where a large portion of electrons was transmitted through the sample, whereas in dark areas fewer electrons had been transmitted.

Now that the theoretical basis for the investigation of PEMWEs has been clarified, the next chapter deals with the practical part of the experiments.

3 Experiment

After the methods were explained in chapter 2, this chapter deals with the actual experimental set-up, or more precisely, the fabrication, implementation and subsequent characterisation of the samples is explained in more detail.

3.1 Ink fabrication

This chapter describes the used materials as well as the chronological procedure used for the fabrication of the catalyst inks.

3.1.1 Catalyst ink and MEA materials

Table 3-1 gives an overview of the components and materials used during the catalyst ink formulation and subsequent CCM and MEA fabrication.

Component/Material	Function	Supplier
Iridium black, 99,8% (metals basis) S.A. > 20 m²/g	Catalyst	Alfa Aesar
1,2-propanediol, 99%, extra pure	Solvent	Acros Organics
Cyclohexanol, 99%	Solvent	Sigma-Aldrich
Cycloheptanol, 97%	Solvent	Sigma-Aldrich
Polyvinylpyrrolidone (PVP)	Surfactant	Sigma-Aldrich
Nafion® perfluorinated resin solution (5 wt% in mixture of lower aliphatic alcohols and 45% water)	Ionomer	Sigma-Aldrich
Nafion® perfluorinated resin, aqueous dispersion (10 wt% in water), EW 1100	Ionomer	Sigma-Aldrich
Sulfuric acid S.G. 1.83 >+ 95%	Cleaning solvent	Fisher Scientific U.K. Ltd
Perdrogen® 30% H_2O_2 (w/w)	Cleaning solvent	Sigma-Aldrich
Emsure® Acetone	Cleaning solvent	Merck KGaA
Ethanol absolute	Cleaning solvent	VWR chemicals
FEP foil (125 μm)	Decal	Goodfellow
PET foil (125 μm)	Decal	Goodfellow
Nafion® N117 (177.8 μm) - EW 1100 - 30x30 cm	Membrane	Ion Power GmbH
Cloth GDE - 0.5 mg/cm² PtC 60% - 20x20 cm	Cathode catalyst	FuelCellsEtc
Bekipor® ST - Ti foil - 2GDL 10 - 0.25 - 56% porosity	Anode current collector	Bekaert

Table 3-1: Chemicals and components for MEA fabrication

3.1.2 Solution preparation

The present solvents of the commercially obtained Nafion® solution were substituted by 1,2-propanediol (PG), in order to remove the influence of the lower aliphatic alcohols and/or water onto the ink formulation. Therefore, the commercial Nafion® solution was put into a glass beaker, where the amount of PG was added to obtain a 25 wt% solution of Nafion® in PG. The mixture was equipped with a magnetic stirrer and homogenised for 5 min at 200 rpm. The beaker was then lowered into a thermocouple-controlled water bath, which was kept at 80 °C by a heating plate, while the solution was constantly stirred until all excess solvents were evaporated. The mixture was then cooled down to room temperature and stored in a plastic screw cap storage bottle.

The Polyvinylpyrrolidone (PVP) powder is similarly dissolved in PG to obtain a 10 wt% PVP solution. Both PVP and PG are added into a glass vial equipped with a magnetic stirrer. The mixture is then homogenised at 400 rpm at room temperature and kept on the magnetic stirrer overnight until all PVP is dissolved and a clear light-yellow solution is formed. The PVP functions as a surfactant and improves the longevity of the CL as it reduces the aggregation likelihood of neighbouring scarce earth metals nanoparticles [48, 49]. In general, the PVP is already quite common in Pt containing inks for PEMFC systems and the positive effect of the additive is also expected for Ir nanoparticles.

3.1.3 Electrocatalyst ink formulation

The Ir black was added into a 5 ml glass vial, which was equipped with a 4.5 mm stir bar. Then the glass vial was tapped onto a hard surface to remove electrostatically charged powder from the glass wall. A gentle nitrogen flow (1 l/min) was used for 30 seconds to remove oxygen from the vial. Following that step, the solvent was pipetted in a fashion that the whole surface area of the powder was fully covered by the solvent. Subsequently, the 10 wt% PVP solution was added. This mixture was dispersed at 800 rpm and left stirring for 10 min on the magnetic stirrer. The dispersion was transferred to the sound-isolating chamber of the ultrasonic processor (Hielscher UP400S) device. The water bath was placed on a magnetic stirrer and equipped with a stir bar to enable a constant circulation of cold water during the ultrasound processing. Then the tip of the sonotrode was steadily lowered into the dispersion to avoid high upward forces onto the sonotrode and until the tip was 1 cm deep submerged in the dispersion. The vial was lowered until the dispersion equals with the water level of the small, cold water bath (⌀ 10 cm) and fixed in this position with a clamp. The amplitude and cycle of the ultrasonic processor was set to 75% and 0.5 respectively and the magnetic stirrer set to 800 rpm. The

ultrasonic dispersion process was operated for exactly 16 min. Subsequently, the desired amount of the Nafion® solution was added to the mixture. The vial was closed and stirred for another 10 min at 800 rpm. The obtained ink solution was kept stirring at 450 - 500 rpm for at least 60 min before further processing.

The total solvent amount was kept constant for all ink formulations, whereby PG was used as pure solvent and in a fixed 50:50 ratio mixture with cyclohexanol (CHEX) and cycloheptanol (CHEP) to obtain these ink solutions. The amount of PVP solution was kept constant at 0.5 g for each ink solution to maintain a content of 2.25 wt% after the solvent was evaporated and a dried CL was obtained. The amount of Ir black was also kept constant for each sample, while the ratio of Nafion® to Ir was adjusted for each ink formulation. The ink with solely PG as solvent was adjusted to obtain 5, 7.5, 10, 15, 23 and 30 wt% Nafion® content in the anodic CL and after the solvent was evaporated from the screen-printed sample. The tested Nafion® contents of the dried CL with ink formulations of 50:50 CHEX and PG encompass 10, 23 and 30 wt%. The investigated CL obtained from the ink containing a 50:50 weight ratio of CHEP and PG had an ionomer content of 10 and 23 wt% in the dried CL.

Inks containing CHEX have been formulated and processed between 25 - 29.5 °C to ensure that the solvent is in liquid form. This is due to the particularity of CHEX, which solidifies when stored or processed at room temperature.

A suitable preselection and identification of promising support materials for the CL was done with the RDE experiments.

3.2 RDE

The supported catalyst samples were calcined at 300 °C for 2 h in a muffle furnace (Heraeus M1100/1) and then crushed with a spatula to obtain a loose powder. The catalyst powder was weighed and put into a 5 ml glass bottle, where it was crushed with the spatula and Milli-Q® water was added to obtain a solution of 1 mg/ml. The glass bottle was sealed with parafilm and sonicated for 10 min.

The measurement was done on the RRDE-3A (ALS Co., Ltd) device. The gold electrode was polished with the PK-3 electrode polishing kit (ALS Co. Ltd). Therefore, the wetted alumina polishing pad was placed on the glass plate and a few drops of 0.05 µm polishing alumina were added. The Au RDE tip was cleaned by placing it at right angle onto the polishing pad and

forming a circular eight motion for 2 - 3 min. The tip was then rinsed for 2 min with DI water and subsequently with Milli-Q® water (18.2 MΩ/cm @ 25 °C). Following this procedure, the tip was placed into an ultrasonic bath for 3 - 5 min and dried with an applied nitrogen flow. The working electrodes were prepared by pipetting an aliquot of catalyst ink (4 µl) onto the 3 mm gold electrode (ALS Co. Ltd) to achieve a catalyst loading of 20 µg/cm^2. The catalyst ink was mounted on the inverted RDE rotating at 50 rpm under an air atmosphere. The rotating speed was gradually adjusted every min (100 rpm/min) until 700 rpm was reached to yield uniform and reproducible thin-films on the Au surface. The catalyst solvents were evaporated during the 30 min air drying treatment while the tip was kept rotating at 700 rpm.

In the meantime, a 50 ml glass beaker was rinsed thoroughly with water. The 0.1 M H_2SO_4 solution was poured into the beaker and closed with the corresponding three-hole cover. An argon flow was applied for 15 - 30 min to remove all solved gases from the solution. The Au counter electrode was rinsed with Milli-Q® water, dried and inserted through the cover void into the H_2SO_4 solution. The hydrogen reference electrode (HydroFlex®) was introduced and fixed into the glass adapter frit, which was itself inserted with its bended neck into the beaker. The electrodes were connected to the potentiostat/galvanostat (Ivium Technologies) as well as to the reference and counter electrode. The dried ink on the RDE tip was mounted as the working electrode onto the RDE device, turned upside down and lowered into the H_2SO_4 solution. The working electrode was kept rotating at 2,500 rpm during the whole measurement to avoid any potential bubble accumulation on the catalyst's surface area. Therefore, the generated oxygen at the electrode surface tip was removed by the fast rotation and argon flux during the measurement.

The cyclic voltammograms were recorded at a scanning rate of 100 mV/s while a measurement data point was taken every 0.1 second between the potential range of +0.05 V and +1.65 V vs. RHE under an argon atmosphere at 25 °C room temperature. All RDE measurements were repeated at least three times to ensure reproducibility.

3.3 MEA fabrication

This chapter describes the chronological procedure following the previously mentioned ink preparation, which was used for the fabrication of the MEA.

3.3.1 Screen printing

The FEP or PET foil (125 µm) was cut into 9.8 x 9.8 cm squares to obtain the decals, on which the ink was printed. The vacuum board was equipped with a mask of the same material as the decal and having a centered opening of 10 x 10 cm. The decal was weighed and put into the void of the gasket onto the vacuum board. The vacuum system of the machine was used for the fixation of both the decal and the gasket to avoid any movement during the printing step. The screen printer (E by DEK; ASM) was equipped with a squeegee (49/265 T/E SQY ASSY Green170; DEK) and a screen mesh (fabric: 265/50/80 mesh/45° Kiwo 30 µm, 8 - 12 µm; Partnertec) with an open void area for coating of 7.1 x 7.1 cm. The printing speed was set to 50 mm/s, while the gap and speed to separate the decal from the mesh after the printing step were set to 3 mm and 1 mm/s respectively. The front and rear pressure was fixed at 7.0 kg. The prepared inks have been stored at 450 rpm on a magnetic stirrer and ultrasonicated for 10 min in an ultrasonic bath (Transonic 700/H; Elma) at a frequency of 35 kHz prior to screen printing. Approximately 1 - 1.5 g (1 - 2 ml) of the viscous ink was applied with a spatula onto the screen about 1 cm in front of the printing void. The vacuum board was then put on the board rail of the screen printer and a screen print cycle was performed. Then the board was removed from the rail, the vacuum turned off and the decal weighed before and after drying at 65 °C to calculate the exact Ir loading of each layer. Three complete screen print cycles have been performed to obtain a CL with the targeted Ir loading of 2 mg/cm². The printed decals have been punched with a 3.1 x 3.1 cm hole punching tool (Hydron Energy) and the obtained four anode CLs have been stored in a plastic zipper bag to protect the surface from dust particles. The screen mesh was cleaned with ethanol and water and wiped dry with dust free paper.

3.3.2 Membrane treatment

The N117 membrane has been cut into 4.3 x 4.3 cm squares. Dusty or otherwise stained membranes underwent the following cleaning procedure to remove any residues from the surface. The dusty squares were boiled in 5 wt% H_2O_2 at 80 °C for 60 min under constant stirring and washed in DI water at 80 °C for 30 min. Following this procedure, the membranes were boiled in 1 M H_2SO_4 at 80 °C for 60 min and afterwards washed in DI water at 80 °C for another 30 min. Subsequently, the washed membranes were dried for 10 min at 65 °C and stored between two FEP foils, which have been cleaned with ethanol and DI water. Already clean and dust-free N117 membranes were not needed to pass through this elaborate cleaning procedure.

3.3.3 Hot-pressing

The upper and lower plate of the hot-press have been preheated to 130 °C. In the meantime, two FEP foils have been cut into 9.0 x 9.0 cm squares. One of these two FEP foils was put on the stainless-steel metal plate (10 x 10 x 1 cm). A PET gasket with a centered 4.5 x 4.5 cm void was put on the FEP foil. The decal with the Ir electrode side-up was weighed and then placed into the void of the gasket onto the FEP foil. The dry N117 membrane was placed onto the Ir electrode and another FEP foil was placed on top of the membrane. Finally, the second metal plate was placed on top of the FEP foil. The exact arrangement of the stack is shown in Figure 3-1.
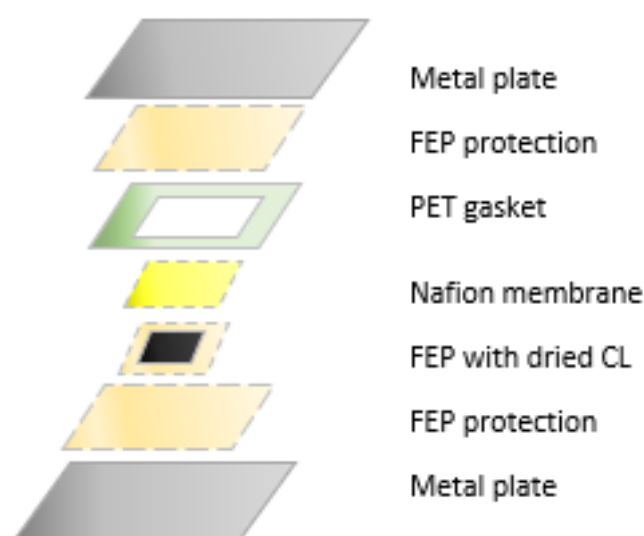
Figure 3-1: Arrangement of the different sheets prepared for the hot-pressing transfer of the CL onto the membrane.

The complete package was placed in the centre of the hot-press. The press was then tightened for 10 min but still without pressure to ensure that the components were heated up evenly to 130 °C. After preheating, a pressure of 3.125 kN/cm² was used for the 3.2 x 3.2 cm square pieces of the catalyst layer. Thus, a force of 32 kN was applied onto the stack plates and hold for exactly 90 seconds. The pressure was then released, the hot-press opened and the stack was removed from the apparatus. The obtained half-cell CCM between the FEP foils was removed from the metal plates and left to cool down at ambient conditions. Subsequently, the FEP foils and the decal were carefully removed. The decal was weighed to obtain the exact loading of Ir at the anode half-cell CCM. This two-layered CCM was stored between two FEP foils in a closed plastic zipper sachet. The steel plates were cooled down in a water bath to room temperature and dried before the next electrode package was assembled and hot-press transferred from the decal onto the membrane.

3.3.4 MEA and electrolyser cell assembly

The gas diffusion layer (GDL) Ti cloth was cut into 3.2 x 3.2 cm squares, cleaned in an acetone-water mixture and ultrasonicated for 10 min. The Ti GDL was then dried on all sides with a strong nitrogen flow for approximately 1.5 min. The commercial gas diffusion electrode (GDE) PtC cloth with a platinum loading of 0.5 mg/cm² was cut into 3.1 x 3.1 cm squares. The sheet resistance of the Ir electrode half-cell was measured prior to the mount of the MEA. In conclusion, the actual MEA was a combination between an anode half-cell CCM and a cathode half-cell catalyst coated electrode (CCE).

The single cell electrolyser stack (EL10, Hydron Energy) was used for the MEA and had an active surface area of 10 cm². The titanium endplates with parallel flow channels have been cleaned with a scrub cleaner pad (Scotch-Brite) and DI water. The residues on the endplates have then been washed with DI water and rinsed thoroughly with ethanol. The surface was air blown to remove any residues of the solvent. Subsequently, the rubber O-rings have been placed into the void of the endplates. The four hexagon-head screws with washers have been placed into the fittings of the anode cell stack housing. A PET gasket (250 µm) with a 10 cm² void was put onto the anode side endplate to prevent leakage during electrolysis operation. The cleaned Ti GDL was put onto the flow channels of the endplate. The Ir half-cell CCM was placed onto the Ti GDL with the shiny side of the membrane upwards. A second PET gasket was mounted onto the cell stack and the PtC electrode was placed with the electrode side onto the membrane. The second endplate was placed onto the backside of the PtC electrode. The four washers and nuts have been placed onto the screws and tightened. The schematic structure of the various layers is shown in Figure 3-1 (see previous page). Only then could the assembled electrolysis cell stack be turned on its side without changing the position of the MEA within, in order to apply a torque of 15 kNm diagonally crosswise to each screw in a first interim stage. With the final torque of 25 kNm, the single flask stack was tightened diagonally crosswise in the same manner.

The assembled cell stack was then placed into the test station and all electrodes, sensors, mass flow in- and outlets were connected to the cell stack. The hydrogen/water outlet as well as the emergency nitrogen flush were connected to the cathode side. The water in- and outlet was assembled onto the anode side as well as the oil cooling in- and outlet. Finally, the electrodes and sensors were connected to the cell. The fully assembled cell stack with all associated connections is depicted in Figure 3-2 (see next page).
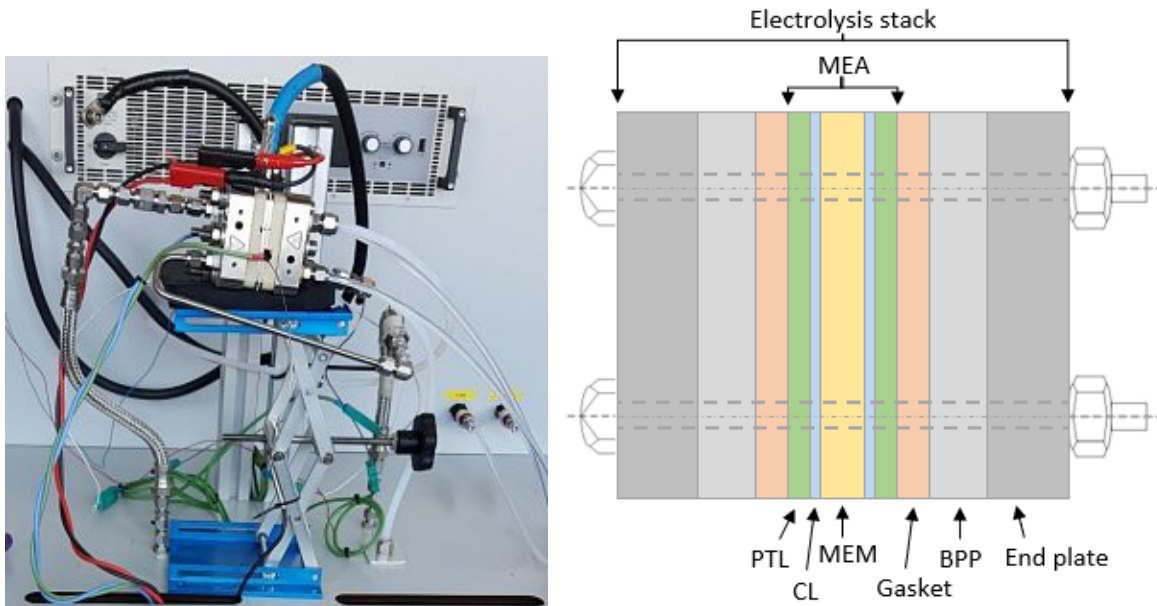
Figure 3-2: Mounted MEA on the left and corresponding schematic structure of the layers in cross-section on the right.

3.4 MEA characterisation

This chapter describes the procedures used for the measurement and characterisation of the various anodic catalyst layers as well as the testing of the mounted MEA in the electrolyser cell.

3.4.1 Sheet resistance

The sheet resistance of the anodic half-cell CCM was measured with the Ossila software package and a four-point probe before the MEA was assembled. The probe spacing was set to 1.27 mm, the target current was kept at 100 µA and the maximum voltage was limited to 7.0 V. The voltage increment was varied in coordination with the sample examined between 0.01 - 0.05 V on the one hand to obtain high data point resolution for the 25 repeats and on the other hand to accelerate the measurement time. The measurement was done on a corner position, in the centre of the probe and for the last measurement the CCM was rotated by 90 degrees and another corner position was tested. Thus, each CCM was measured at three different locations to obtain the average sheet resistance. The resistance was used as an indicator for the expected MEA performance and to get an impression of the homogeneous catalyst surface coverage on the membrane.

3.4.2 Conditioning of the electrolysis cell

The cell stack in the electrolysis test station was initially heated to 40 °C before the measurement was recorded. As soon as 40 °C were reached, the security flushing nitrogen flow was turned off and the inlet and outlet valves for the water flow were opened. The heater for the water feed flow was set to provide an 80 °C hot inlet stream. When the water stream started

to heat up, the maximum of the voltage was set to 2.1 V, while the maximum electrical current was limited to 30 A. The upper limit of the potential was set to prevent the cathodic electrode cloth from being damaged by carbon corrosion. The measurement was started and the cell kept running for about 18 h before the electrochemical characterisation was performed. The IV curve was taken and the cell was given enough time to stabilise to the applied 2.1 V before the impedance measurement at 2 A and 5 A was recorded according to the protocol below.

3.4.3 IV curve

The IV curve test protocol was implemented so that the measurement was started at 25 A and then reduced by one ampere each cycle until 0.5 A was reached. Then the current was ramped up again to reach the original 25 A. The current was measured by an amperemeter, which was connected in series. During the measurement, the resulting voltage was recorded by the voltmeter connected in parallel.

3.4.4 Impedance measurement

For the impedance measurement the test system's current was stepwise reduced from the original 30 A to 10 A. This took approximately 10 min. In the second step the current was further reduced to 5 A, which took not more than 2 - 3 min to avoid a drastic current drop. The electrodes of the impedance measurement device (Zahner PP200 & IM6ex) were connected to the electrolysis cell stack. The device was started in galvanostatic mode and 5 A were applied to the cell stack. After this procedure the power of the cell stack was quickly switched off. This procedure was followed to avoid unnecessary changes and performance losses due to the abrupt shutdown and restart of the electrolysis cell operation. The cathode connection of the test station to the cell stack was removed to exclude back noise and to obtain data without noisy overlays. The device's measurement range was set between 10 kHz and 100 mHz and the impedance measurement was done at 5 A and 2 A. The Nyquist plots were saved and the resulting data exported. After the second measurement the cathode was reconnected to the cell stack and the test station was restarted. The impedance device was then turned off and the impedance electrodes were disconnected, while the previously removed test station sensors were reconnected to the cell stack.

3.4.5 Cell station shutdown

After completing all of the aforementioned measurements, the system was returned to open circuit conditions. Thus, the gas lines were purged with nitrogen for at least 10 min. The heating device's setting was then reduced to zero to allow the system to cool down to ambient conditions, and the valves were opened to remove the system back pressure as well. The cell

stack lines were disconnected from the test station and the cell housing disassembled. The compressed MEA package was removed from the electrolysis cell and stored in a plastic bag for later analysis.

After the procedures of the conducted experiments have been described, the next chapter presents the results and a further discussion of the obtained data.

4 Results and Discussion

The findings of this study, namely the ionomer loading characterisation, the catalyst ink optimisation through proper solvent choice, the CL fabrication and the performance of the resulting electrolysis cell, are presented and discussed in this section. The RDE tests were conducted with the three ink variations: Ir black, Ir@ATO and Ir@TiB$_2$. The activity of these samples is compared to the reference of commercially available IrO$_2$@TiO$_2$ (Umicore).

The first main aspect of the work deals with the findings concerning the optimised process conditions to maintain a reproducible anode half-cell CCM fabrication. The reproducibility was ensured by two independent screen prints of each ink formulation and subsequently testing of at least two of these screen printed CLs. The following part discusses the electrolyser results of the dual tested MEAs, which have been conducted with a maximum operation potential of 2.1 V and a cell area of 10 cm^2. The scope for the MEA test included the samples PG-5, PG-7.5, PG-10, PG-15, PG-23 and PG-30, whereby the attached number indicates the ionomer content within the dried CL. The ink formulation for the   PG-23 served as the reference material. In the binary ink samples half of the solvent´s amount of PG was replaced by the respective, categorising solvent. These samples were labelled as CHEX-10, CHEX-23, CHEX-30, CHEP-10 and CHEP-23. The potentiostatic polarisation mode was chosen to ensure a more linear deterioration curve compared to the progression of the galvanostatic operation mode. IV curves were conducted after sufficient conditioning time to effectively compare the different CLs obtained under the same operation conditions of 1 bar and 80 °C. The contribution of the specific CL's internal resistance behaviour was examined by the EIS measurement. BET values for the commercial Ir black catalyst have shown a surface area of merely 15 m^2/g compared to the available data from the manufacturer that listed a surface area of 20 m^2/g.

First, the results of the preliminary investigations of the anodic CL's ink formulation from RDE experiments are given and discussed.

4.1 RDE

The Ir catalyst was mixed with either TiB$_2$ or ATO and half of the catalyst amount was calcined at 300 °C for 2 hours. The calcined sample was crushed and blended with Milli-Q$^®$ water to obtain solutions of 0.2 mg/ml and 0.3 mg/ml. Originally there was a larger comparative sample examination planned (i.e. Ir@TiB$_2$, TiB$_2$, IrO$_x$@TiO$_2$, Ir@ATO, Ir black) but both time

limitation in testing capacity and work restrictions imposed due to the COVID-19 pandemic complicated these attempts. Therefore, the scope of this section was adjusted to these circumstances. Figure 4-1 (see next page) depicts all prepared solutions after several days of settling time. The catalyst material in the samples Ir@ATO and Ir black settled completely and it accumulated on the glass bottom. The other catalysts remained in the aqueous solution with partial but minor segregation.

Figure 4-1: Prepared catalyst solution for the RDE measurement

The catalyst loading was kept at 16.5 µg/cm² for all samples, whereas the total amount of Ir was estimated based on the manufacturing process to be 10% for all samples with TiB_2 or ATO as the support material. The reference sample from Umicore had a ratio of 75% IrO_2 and 25% TiO_2. The samples investigated are given in Table 4-1 (see next page). ATO was chosen since in other reports the support material was described as highly conductive but otherwise deemed too unstable for long-term operation [50, 51]. On the other hand, TiO_2 supports are proven to be highly corrosion resistant, although the low electron conductivity of TiO_2 leads to unfavourably high iridium loadings to obtain suitable performance values [52]. Thus, it was promising to test TiB_2 as support material in PEMWE applications as the supported Pt catalyst showed highly increased stability values during operation in PEMFCs compared to the aforementioned supports [53, 54, 55].

Component/Material	Description	Notation
Iridium black, 99,8% (metals basis) S.A. > 15 -20 m²/g	Ir black nanoparticles	Ir black
75 wt% Ir on 25 wt% TiO_2	Ir black supported on TiO_2 (Umicore)	Ir@TiO_2
10 wt% Ir on 90 wt% TiB_2	Ir black supported on TiB_2 (untreated or calcined)	Ir@TiB_2
10 wt% Ir on 90 wt% ATO (10-20 nm)	Ir black supported on Sb_2O_3/SnO_2 (untreated or calcined)	Ir@ATO

Table 4-1: The investigated catalysts and associated abbreviations

The RDE test was used to screen for promising support candidates. The simpler and quicker measurement accelerates this endeavour, although only subsequent MEA tests can provide more reliable activity and durability results under real operation conditions for each new catalyst material. Moreover, the prepared inks with PG were too viscous to pipette exactly 4 µl with the available laboratory equipment onto the tip of the RDE disk. Thus, it was impossible to coat the GC working electrode with the actual catalyst inks. However, this could be remedied in future works with larger amounts of the observed samples, high precision syringes or improved coating techniques. In subsequent measurement series it may be possible to pre-select ink compositions formulated for screen printing with the RDE measurement to accelerate the development of PEMWE inks, while considerably reducing the necessary sample size and the required Ir amount.

Figure 4-2 shows the results obtained from the CV curves. The adsorption of hydrogen occurs at potentials between 0 V and 0.35 V versus RHE. Possibly present Ir is oxidised to Ir (III) within the potential range of 0.4 - 0.8 V. The obtained Ir (III) is then oxidised to Ir (IV) within the potential range of 0.8 - 1.2 V [56]. The surface activity was the highest with the pure Ir black sample, which is not surprising as this sample consists of solely commercial catalyst material. The further activity performance achieved is in close alinement with the decreasing amount of Ir in the samples, although ATO samples outperformed TiB_2 samples. This can be explained by the higher electron conductivity of ATO. All calcined samples performed slightly lower than the corresponding untreated samples. This is likely due to the denser structure of the calcined samples and possibly partial oxidation of Ir black to IrO_2 during the process.

More interesting are the results of the mass activity (MA), since the results have been standardised to the expected Ir loading of the samples. Unfortunately, the more comprehensive and meaningful comparison with various Ir loading could not be carried out to the full extent

due to aforementioned time constraints. Nevertheless, a first estimate can be made based on the available data. According to the results, ATO showed the highest MA but this will probably be accompanied by a serious reduction in long-term stability. Ir black and TiB_2 supported Ir ($Ir@TiB_2$) have been in the same performance area. This is utterly remarkable as the samples with TiB_2 had 10 times less Ir content. This might be in turn due to the contribution of TiB_2 as a thermal and electron conductor. The commercial sample showed the lowest activity, mainly because TiO_2 does not contribute to the electron conductivity and is considered as an insulator at room temperature. All in all, TiB_2 could be interesting as support for PEMWEs, as the material is likely to have a good trade-off between stability and activity. However, long-term tests and charge optimisations are still pending in connection with the ideal ionomer content and the dispersant mixture used.
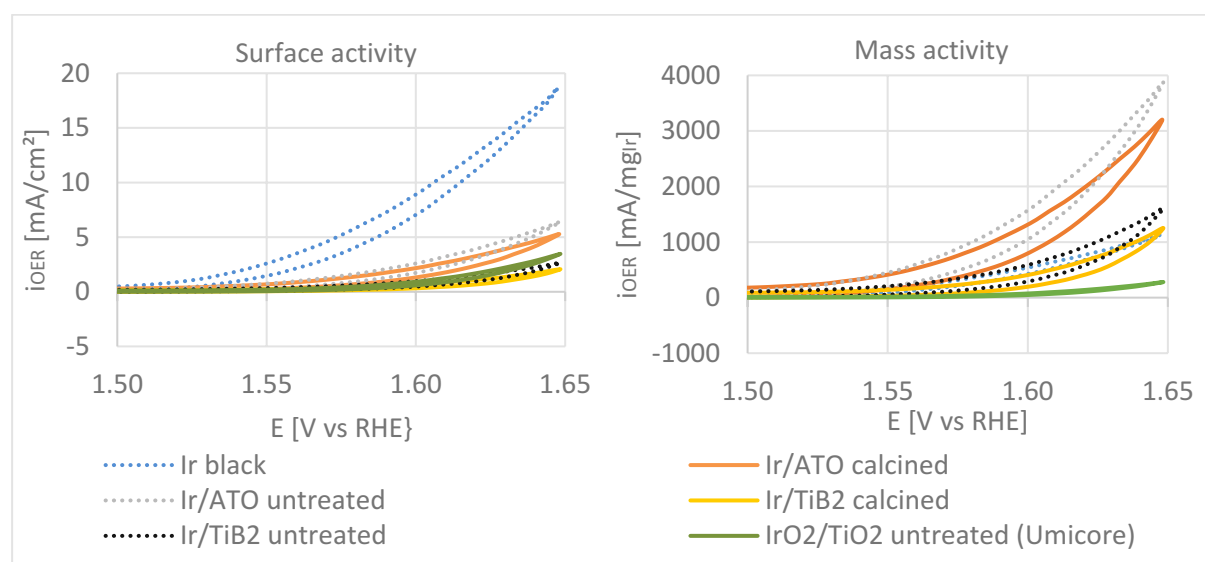
Figure 4-2: OER surface and mass activity obtained from the RDE cyclic voltammetry results, tested at 25 °C, RDE rotated at 2,500 rpm.

The following chapter is dedicated to the actual examination of the encountered influences on the CCM fabrication process.

4.2 CCM fabrication

The targeted Ir loading of the anodic CLs was 2 mg/cm², which corresponds to the state of the art of built PEM electrolysers. The ink formulations contained the same amount of Ir catalyst and PVP solution as a surfactant agent, while the ionomer and dispersion solvents were varied. The inks were screen printed onto decal foils before drying and the subsequent transfer onto the N117 membrane.

4.2.1 Dispersion solvents

The solvent amount of the prepared inks resulting in CLs with 10 wt% Nafion® content was kept at 73.5 wt% and 68.25 wt% for inks prepared for CLs with a targeted Nafion content of 30 wt% after drying. The total solvent amount of the ink samples was kept constant for all inks to preserve the ratios of the formulation protocol and to obtain similar loading values per printed layer. Thus, the printing parameters were kept constant for all ink samples.

CHEX and CHEP have a cyclic structure and only one hydroxyl group, whereby PG has a linear structure and two hydroxyl groups. This cyclic structure with one hydroxyl group lowers the polarity of CHEX and CHEP compared to the linear structure of PG. Moreover, the two hydroxyl groups of PG provide more possible sites for hydrogen bridge bonds with the sulfonated groups of the ionomer than solvents with only one hydroxyl group (e.g. CHEX and CHEP). All in all, the intention was to combine the advantages of both solvent types into the binary solvent mixtures. At the same time, a drastic change in the formulation recipe was avoided to ensure the printability of the inks.

Initially, CHEX and CHEP inks were prepared with a mass ratio (x:PG) of 80:20, 62:38 and 50:50. This was deemed unfavourable for observing only the effect of the ionomer content onto the electrolysis performance. Therefore, all MEAs tested with CHEX and CHEP inks had a mass ratio of 50:50 PG and were compared with samples containing solely PG. In other words, this means that the same amount of PG and CHEP or CHEX was used for the binary solvent mixtures. The physical properties of the investigated solvents are listed in Table 4-2 (see next page) as well as the adjusted criteria for screen printing based on the work of Wang et al. [57] are given. In general, the choice of dispersion solvent effects the drying time as well as the ionomer distribution due to the modified physicochemical properties of the ink. The solution form (i.e. $\varepsilon > 10$) possibly improves the triple phase boundary, while the precipitation form (i.e. $3 < \varepsilon < 10$) reportedly leads to an improved deposition behaviour on the catalyst particles [57, 58]. Nevertheless, all solvents yield in homogeneously distributed inks without any observed segregation processes, as the bonding of the ink was further ensured by continuous stirring.

Solvent carrier	Dielectric constant [-]	Viscosity (@ 20 - 25 °C) [cP]	Boiling point [°C]	Vapour pressure [Pa]
Cycloheptanol	13.5	51.5 - 53.6	185	26.7*
Cyclohexanol	15.0 - 16.4	41.0 - 56.5	161	133.0
1,2-Propanediol / Propylene glycol	28.7 - 29.5	43.4 - 59.9	187	10.6
Criteria for screen-printing	> 10	16 - 60	150 - 230	5 - 150

*…estimated value

Table 4-2: Criteria and physical properties of the cyclic and dialcoholic dispersion solvents [57, 59, 60]

Figure 4-3 shows the hot-transferred CLs with 10 wt% ionomer content, whereby the samples with CHEX and CHEP have a porous structure with uncoated voids. This might be influenced by the interactions of the decal with the solvents during the drying process. These voids are larger and more numerous in the CHEX sample than in the CHEP sample. In comparison there is also the sample with PG depicted, whereby no void formation was observed. However, the porous structure had no negative impact onto the performance during electrolysis as shown later.

Figure 4-3: Comparison of the CCMs with 10 wt% ionomer in the dried CL. *A:* 50:50 CHEX:PG, *B:* PG, *C:* 50:50 CHEP:PG

4.2.2 Influences on screen print homogeneity

The printing took place at ambient pressure environment conditions within a temperature range of 22.0 - 29.5 °C and the air humidity was within 53.0 - 73.0%. CLs printed on the same day as ink preparation showed overall better performance and homogeneity than when screen printing was performed on subsequent days after ink preparation. Thus, it is crucial to limit the storage time of the inks because it can lead to unfavourable ageing phenomena of the ink [61]. Whereas the ionomer induced particle size of the dispersed catalyst and the ink stability might

be affected by polymerisation and/or depolymerisation phenomena as well as deposition segregation effects during ultrasonication and magnetic stirring. Furthermore, it was observed that exchanged squeegees of the same manufacturer and dimension (i.e. 170 mm), even after automatic adjusting, still resulted in an inhomogeneous print coverage. This is depicted in Figure 4-4, where triangular shapes with less applied ink are repeatedly apparent at the bottom and a continuous line is visible at the right border. The effect was limited by alternating front and back strokes of the opposing installed squeegees. Nevertheless, to exclude the varying contribution from the different squeegees on the screen printing result, the same pair of squeegees of Figure 4-4 B was used for all tested samples.
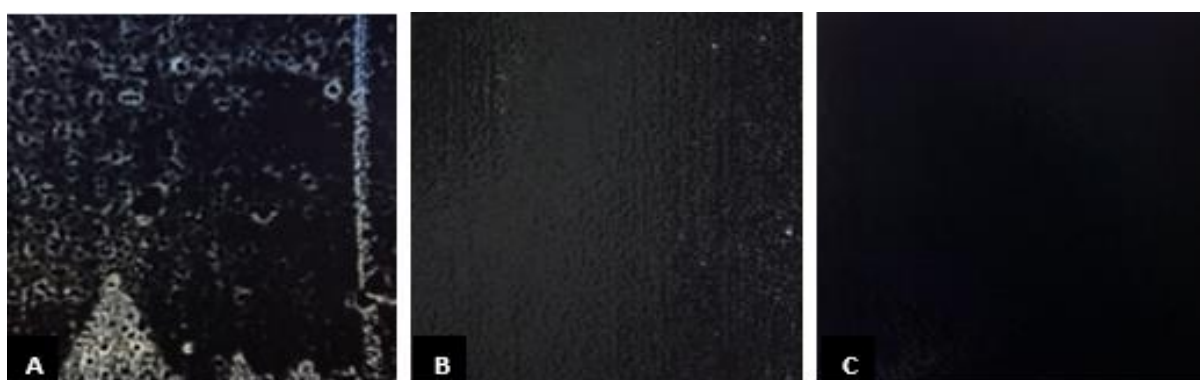
Figure 4-4: *A:* **Dried CHEP sample (Nafion 10 wt%), printed with one stroke of the non-uniform applying squeegee,** *B:* **Wet PG sample (Nafion 15 wt%), printed with the uniform applying squeegee,** *C:* **dried CL obtained from PG (Nafion 15 wt%) printed three times with alternating front and back strokes.**

Another specificity was observed with the 80:20 CHEX:PG inks. The effect was especially pronounced for CLs with a Nafion content of 10 wt%. The wetting of the complete surface was not attainable with FEP foils due to strong phobic interactions between the ink and the hydrophobic surface of the decal. Therefore, the CHEX ink mixtures with 10 wt% Nafion were printed on PET foil instead. Figure 4-5 shows the effect of the decal material onto the spreading of the ink. In conclusion, no homogeneous coverage was achieved with the FEP foil depicted in Figure 4-5 A compared to the homogeneous coverage on PET foils in Figure 4-5 B.
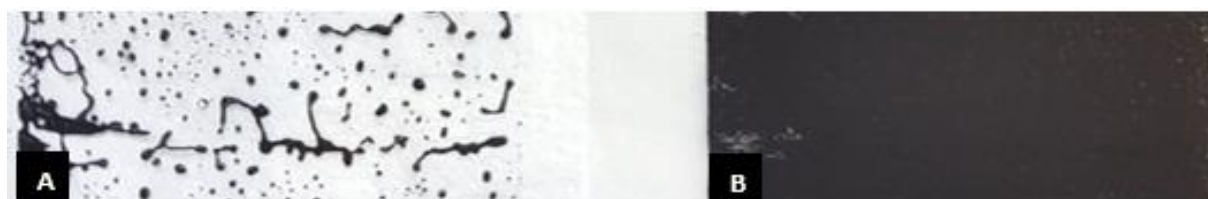
Figure 4-5: *A:* **Mass ratio 80:20 CHEX:PG ink inhomogeneous ink distribution on FEP foil,** *B:* **Mass ratio 80:20 CHEX:PG ink printed on PET foil**

However, if the mass ratio of the binary solvent mixtures was fixed to 50:50, no problematic behaviour of the CHEP samples was apparent. Consequently, PTFE or PET decals were better suited for samples with a weight ratio of 80:20 CHEX:PG, as the used FEP decals resulted in a phobic interaction between the decal and the catalyst ink. In general, the transferability during hot-pressing was improved when FEP decals instead of PET foils were used.

4.2.3 Drying parameters optimisation

The drying conditions were found to largely define the obtained CL's surface homogeneity, crack formation and ageing during storage of the dried samples. The first batch of PG samples was dried in an incubator (Memmert) at 85 °C for 10 min after each layer and for further 60 min after the last printed layer. The air flow was set to 100% to enable fast evaporation of the solvent. The dried CL appeared to be intact and each print was stored in a dust-free plastic bag. The appearance of the CL remained homogeneous for about one week. However, after hot-pressing there was already pronounced crack formation observed. After the first fortnight cracks began to become optically visible even before the hot-transfer onto the membrane.

Raised drying temperatures of 90 °C resulted in instantaneous destruction of the CL's structure. Parts of the CL flaked off from the decals during the drying treatment and on the next morning the CL was completely destroyed due to proceeded crack formation and the detachment of large areas from the decal. A reduction of the drying temperature to 65 °C improved the storability of the samples while cracking during the hot-press treatment remained a main concern. The reduced oven temperature resulted in a drying time of 30 min after each layer to fully dry the printed CL, and the additional drying time after the last layer was reduced to 30 min as well. In another attempt to decrease crack formation and avoid inhomogeneous CLs, the air flow during drying was initially reduced to 20% and subsequently to 10%. Especially the air flow was found to be detrimental for the integrity of the CL. This finally led to improved half-cell CCMs with stretches of a continuous anodic CL even after hot-press transfer.

Figure 4-6 (see next page) demonstrates the obtained cracking behaviour of the dried CL. The area of the continuous coverage was substantially increased from D-E as the dominant air flow of the drying chamber was set to 0% and hard plastic panels were put onto the upper and lower drying grate to limit the unwanted air flow. The printed sample was then inserted onto the drawer in the cavity between the plastic panels, and centred on the lower plastic panel to further reduce any influencing effect of the convection flow within the drying chamber. These efforts led to a fully homogeneously distributed CL. Furthermore, the drying time was adapted to the

varying ink compositions since CHEX and CHEP have lower boiling points and the higher vapor pressure leads to accelerated drying than when solely PG was used as the predominant solvent. Table 4-3 (see next page) lists the specific drying conditions for each ink. Both drying temperature and air flow were kept at 65 °C and 0% respectively for the MEA samples tested. Deviations from these parameters are explicitly marked if applicable.
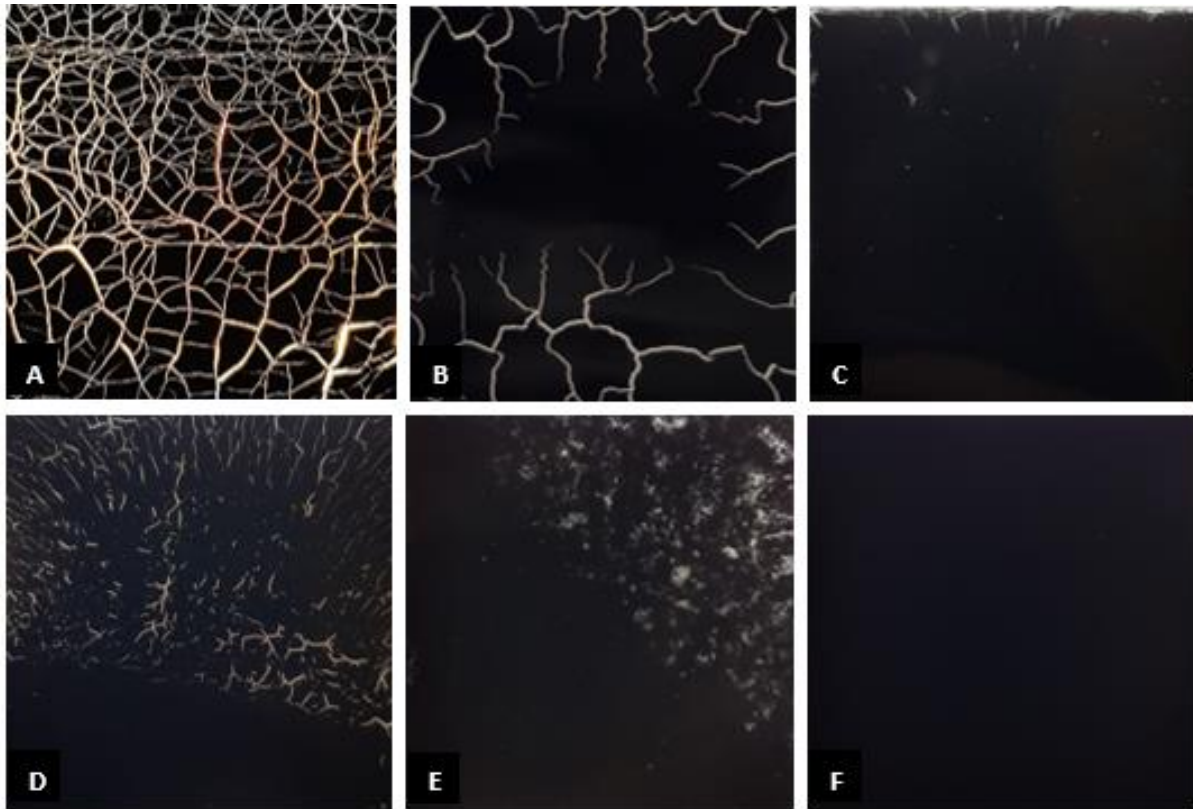
Figure 4-6: *A:* **Cracking occurred instantly after the drying chamber treatment due to high temperatures;** *B:* **Extended crack formation, initial origin of the cracks are lateral cut surfaces of the sample due to storage on the FEP decal;** *C:* **Negligible crack formation on the upper cut surface of the PG samples due to timely transfer from the FEP decal;** *D:* **Curvatures of the foil-covered drying plate led to inhomogeneous drying behaviour while the increased drying temperature of 85 °C resulted in crack formation;** *E:* **Curvatures of the foil-covered drying plate led to inhomogeneous drying behaviour while the adjusted drying temperature of 65 °C prevented crack formation during hot-press transfer;** *F:* **Homogeneous CL without any visible crack formation due to adjusted processing.**

Dispersion solvent	Drying time after each layer [min]	Additional drying time after last layer [min]	Drying chamber temperature [°C]	Air flow [%]
PG-xx	30	30	65	0
CHEX-xx	15	15	65	0
CHEP-10	25	25	65	0
CHEP-23	15	25	65	0

Table 4-3: Realised drying parameters of the different ink formulations tested in the electrolysis cell.

4.2.4 Hot-press transfer

Hot-pressing remains a crucial step in transferring the printed CL from the decal onto the actual proton-conductive membrane, insofar as the CL was not printed directly onto the membrane. Thereby, the type of the decal, the composition of the CL and the pressing conditions have a significant impact on the completeness of the transfer process. Thus, these three factors influence the reproducibility and the obtained number of poorly transferred CLs, which can be regenerated but then have to be reproduced according to the aforementioned steps. Whereas a complete transfer enables a fast and cost-effective production method for high quality and quantities of CCMs. Previously, ink samples were transferred onto PTFE foils. This resulted often in insufficient transfer ratios, while incompletely transferred samples raised reproducibility concerns. Therefore, FEP decals were used instead of the PTFE foils, which resulted in residue-free decal transfers for all samples with an ionomer content of 15 wt% and above. This represents a considerable improvement as PTFE decals still had issues with samples containing the reference 23 wt% Nafion® ionomer in the dried CL. Figure 4-7 demonstrates the effect of the ionomer content of the CL onto the transferability.
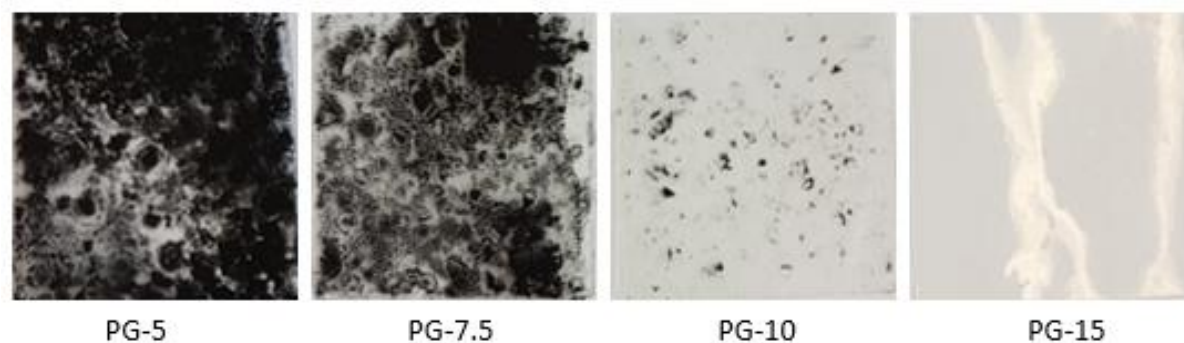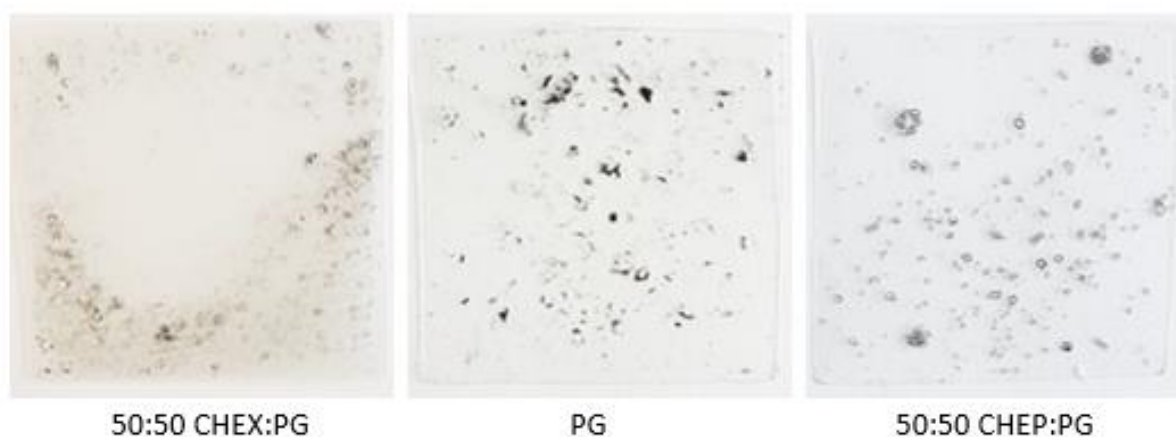

Figure 4-7: Comparison of the catalyst residues remaining on the decals after hot-pressing transfer: All samples used pure PG as dispersion solvent, while the ionomer content varied from 5 - 15 wt%.

It became apparent that a higher ionomer content improved the transfer completeness from the decal. To counteract the transfer problems encountered with CLs containing only 5 and 7.5 wt%

ionomer, the hot-press conditions were varied. Higher temperatures of 140 °C and longer pressing times led to a deterioration of the transfer as more catalyst remained on the decal. Therefore, the preheating time was reduced to 9 min and the application time of the pressure was reduced to 1 min. This resulted in at least 20% more catalyst transfer than with the conventional conditions listed in Table 4-4 (see below). An additional performed transfer proved that the adjusted hot-press conditions were also sufficient for the complete transfer of the PG-15 sample. This experiment verified that 1 min pressurising at a pressure level of 3.125 kN/cm² (i.e. 32 kN for 10 cm² CL) can be used for samples with a higher ionomer content as well. Moreover, the gentler conditions may improve the sample's performance as the heat-sensitive Nafion® membrane is exposed to high temperatures for a shorter period of time. This can possibly improve the performance or extend the cell's operation time as well.

Dispersion solvent	Preheating time [min]	Pressurising [s]	Hot-press temperature [°C]	Pressure [kN/cm²]
PG-10 – PG-30, CHEX-xx, CHEP-xx	10	90	130	3.125
PG-5; PG-7.5	9	60	130	3.125

Table 4-4: Hot-pressing parameters during the transfer from the decal to the N117 membrane.

Otherwise, the solvent's choice had an insignificant effect on the transferability. In Figure 4-8 samples with PG are compared to both binary solvent mixtures with weight ratios of 50:50, where all samples had the same ionomer content of 10 wt%. Therefore, the dominant factor for the transferability focusing on reproducibility was found to be the ink solution's ionomer content.

50:50 CHEX:PG   PG   50:50 CHEP:PG

Figure 4-8: Comparison of the catalyst residues remaining on the decals after hot-pressing transfer: All samples have an ionomer concentration of 10 wt%.

In conclusion, the limitation or complete avoidance of crack formation and further crack enlargement during the transfer process was achieved by the combined improvement of the drying conditions with the use of an additional PTFE mask between the FEP foils during the hot-pressing transfer. The additional mask even led to the partial restoration of the layer's integrity of previously printed samples, which had cracked during the rapid removal of the solvent. This is due to the observation that two adjacent crack fronts were rejointed and the gap was filled through the hot-pressing process. Thus, a homogeneous surface was partly restored. The usage of the mask alone and without applying adjusted drying conditions could already solve the homogeneity concerns induced by minor stress cracks. However, the issues with larger cracks remained since larger cracks or even whole missing flaked-off patches would still lead to incompletely coated membranes. Subsequently, this would result in lower performance and reduced hydrogen yields. In general, the larger drying cracks caused by unfavourable drying conditions were preserved or even aggravated during hot-pressing (see Figure 4-9 on the next page). Therefore, the prevention of these cracks during the drying process is crucial as only the combined approach with the mask led to satisfactory and reproducible qualities of the CL. This endeavour enabled the following comparative study of the ionomer's and dispersion solvent's influence onto the performance of the electrolysis cell to obtain higher current densities. In a next step, this ensures that the iridium loading in the anodic CL can be effectively reduced, while the specific hydrogen yield per catalyst quantity (i.e. MA) can be increased.
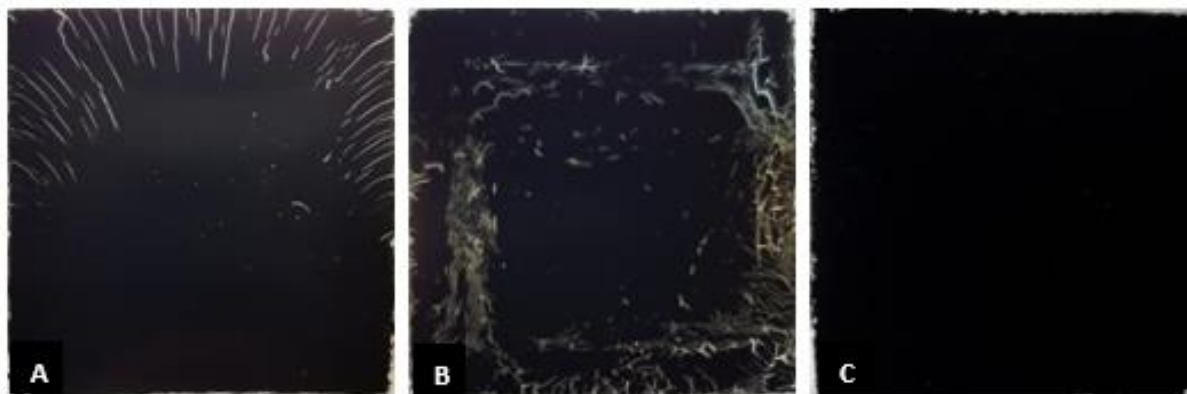
Figure 4-9: *A and B:* **Obtained CCMs with visible drying cracks and inhomogeneous structure caused by unfavourable pressure distribution due to uneven sealing;** *C:* **Ideally obtained structure of the CCM due to suitable processing.**

Now that the optimisation of the manufacturing process has ensured a consistent quality of the CL, the next chapter is dedicated to the electrochemical characterisation of the MEA.

4.3 MEA performance testing

In this chapter, the results of the four testing methods of the MEA performance characterisation are presented and discussed in more detail.

4.3.1 Conditioning and disassembly

Generally, 18 h should have been sufficient to obtain a constant operation current of the electrolysis cell at the applied potential of 2.1 V. Most tested samples reached this equilibrium state at 80 °C within the first 3 h. The corresponding operation conditioning time graphs are shown in the Appendix 10.1 on page XIX. Within the first hours of the potentiostatic conditioning any solvent residues, that may have been present after the drying procedure, should have been completely removed from the CCM's surface. The six conditioning time graphs in the Appendix 10.1 depict the curves of the current, voltage and temperature of all samples over the operation time. The potentiostatic polarisation curve of the current is depicted over 16 h operation time, while only the first 5 h are depicted for the other two parameters since the curves show no major changes over time.

It is remarkable that not all samples of the different ink formulations reached a constant operation mode. The PG samples with 10 and 30 wt% ionomer did not reach the stable operation state. However, PG-10 showed an increasing trend, while PG-30 showed a gradually decreasing activity after an operation time of just 8 h. This was also observed for the CHEX-30 sample, where the effect of the higher ionomer content was even more pronounced and resulted in a steady deactivation. In contrast, the CHEX-23 sample showed an increasing trend. The conditioning was limited to 18 h to ensure that the comparison of the samples could be carried out at the same time and due to the project´s general time limitation. The maximum activity of the CHEX-23 and PG-10 samples could therefore be even higher than listed in this report. The exact cause of this behaviour could not yet be established in the scope of this work. The samples CHEX-10, CHEP-10 and CHEP-23 as well as the remaining PG samples (i.e. PG-5, PG-7.5, PG-23) reached the steady-state operation mode and its maximum activity during the given conditioning time. The MEAs obtained with CHEP-10 and CHEP-23 CLs reached the stable operation already after 2 h and remained constant on a high, resulting current output of 30 A and 25 A respectively. This shows that these two CLs are maintaining a higher electron conductivity and mass transport derivable from the higher potentials. The activity difference between the MEA samples is likely caused by more accessible active sites, which in turn is induced by higher open void volume in the CL and due to the fact that protons are transported more effectively from the PTL/CL interface through the ionomer network to the membrane.

An interesting observation was that samples with higher ionomer content took longer to reach the initial constant operation mode. This can be explained based on the fact that the higher ionomer content results in thicker CLs. An improved, non-destructive method to simultaneously obtain the thickness and equivalent weight distribution of the ionomer would have been achieved by confocal Raman microscopy [62]. However, this method was not available at the time of the analysis and the thickness of the CL was measured with the SEM equipment. Thus, the thickness was obtained from four distinct sites on the SEM images, which are depicted in Figure 4-10 (see next page). The PG-10 sample had an average thickness of 3.04 µm, while the reference PG-23 sample's average thickness was 6.55 µm. The density of Nafion® amounts to 1.98 g/cm³, while the density of iridium was 22.65 g/cm³. This means that thinner CL can be achieved with lower ionomer contents resulting in lower ohmic resistance during electrolysis operation.

The ionomer content also affected the disassembly state of the tested MEA stack. The ionomer content of the PG-30 samples was too high for the chosen catalyst material. This resulted in the excess ionomer being transferred to the Ti PTL, leading to the adhesion of parts of the anodic CL to the PTL. Subsequently, this makes the reusability of the PTL and the recycling of the CL more difficult. The visible longitudinal imprint on the PTL was caused by the BPP, as the stripes were a perfect replica of the flow channels. In contrast, the lower ionomer content of the PG-10 sample did not cause the excess ionomer of the CL to be transferred to the PTL. Therefore, the surface of the Ti PTL remained metallic. Furthermore, this indicates that the structure of the CCM remained intact in contrast to the aforementioned PG-30 sample. Thus, a reassembly becomes more complicated due to the remaining residues, while the homogeneity and integrity of the CL were impaired. These findings prove that the samples with optimised ionomer content can be disassembled and easily reassembled with renewed CCM or PTL, while an additional cleaning procedure would be needed for the samples with an excess of ionomer to remove the residues from the Ti fabric.

After the optical analysis, the next subchapter is dedicated to the electrical evaluation of the investigated PEMWE samples.
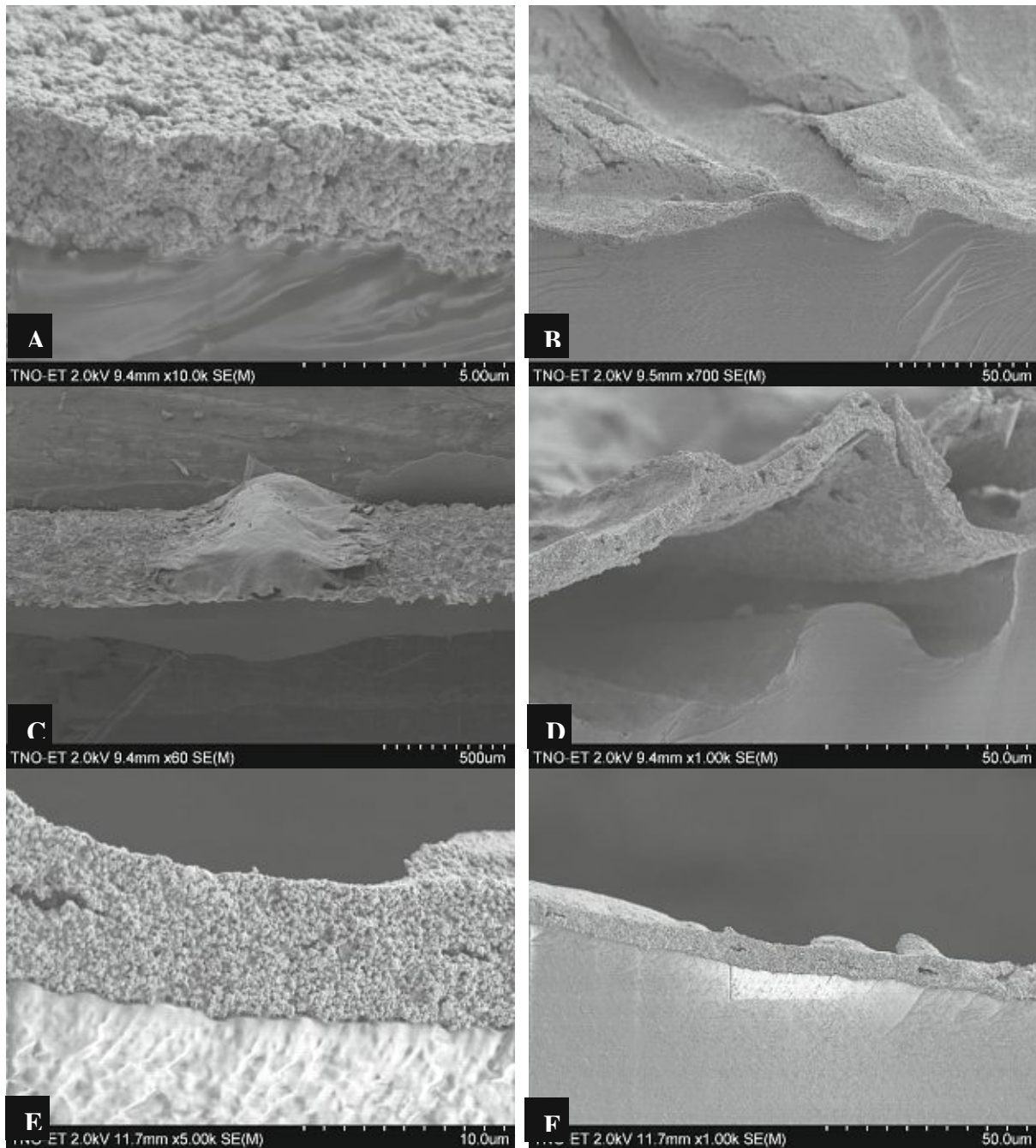
Figure 4-10: SEM images of the Ir catalyst layer on the CCM at lower magnification (5 - 500 μm). A - C depict the sample PG-10, while D - F show the sample PG-23. The SEM images were taken after 18 h MEA operation in the single electrolyser cell stack.

4.3.2 IV curves

The targeted irdium loading of exactly 2.00 mg/cm² was hard to achieve for all samples due to remaining catalyst residues during the hot-transfer process. The Ir loading of the samples was between 1.66 and 2.42 mg/cm². To ensure the comparability of the CL, the Ir loading was normalised to 2.00 mg/cm² in order to limit the influence of the varying iridium content of the samples onto the performance (see Table 4-5 on the next page). Although the essential sequence

of the samples remained in the same order, the difference between the samples was more elaborated and allowed for easier interpretation.

Sample code	Ir loading [mg/cm²]	Lateral cond. [mS]	V at 1 A/cm²	V at 2 A/cm²	Slope of the IV curve [-]
PG-5	1.66	2.29	1.694	1.892	0.198
PG-7.5	1.71	3.51	1.692	1.879	0.188
PG-10	1.83	0.30	1.696	1.910	0.214
PG-15	2.05	1.82	1.710	1.917	0.207
PG-23	2.02	0.54	1.745	2.025	0.280
PG-30	1.95	0.43	2.068	ND	0.412
CHEX-10	2.05	7.91	1.694	1.894	0.200
CHEX-23	2.08	1.85	1.740	1.981	0.240
CHEX-30	2.42	0.34	1.985	ND	0.355
CHEP-10	1.88	4.83	1.677	1.867	0.190
CHEP-23	1.91	0.77	1.747	1.989	0.242

Table 4-5: Collection of the averaged values from the actual IV curves data.

The originally obtained IV curves are given in the Appendix 10.2 on page XXI. At least two samples were tested for each ink formulation in two independent cell stations to ensure repeatability and to obtain the averaged potential curves. Table 4-5 (see next page) lists the most significant parameters obtained from the averaged IV curves during the gradual increase of the current levels. The increasing trend was chosen to exclude the background noise observed during the measurement with decreasing current steps. The potential's safety limit was set to 2.1 V during the elctrolysis operation mode and the cell was kept at a constant temperature of 80 °C. As soon as the maximum voltage was reached, the measurment series was interrupted and the electrolysis cell kept operating at 2.1 V for 2 - 3 h before the EIS measurement was started. It was particularly noteworthy that samples with 30 wt% were not able to reach a current density of 2 A/cm² as these operation conditions would already exceed the maximum voltage limit due to the high internal overpotentials.

Figure 4-11 (see next page) shows the influence of the Nafion® content onto the performance of the whole series with PG as the dominant dispersion solvent. The differences in performance between the individual samples became more pronounced the higher the applied amperage was set. Only PG-30 performed significantly worse than the reference probe. The reference for the performance comparison was again the PG-23 probe. In another experiment, the operating

potential of the PG-23 sample was maintained for a further four consecutive days, whereby no significant changes in the resulting IV curves were observed. Therefore, a stable operation can be expected for at least five days. This meant that some samples were conditioned over the weekend without affecting the results obtained.
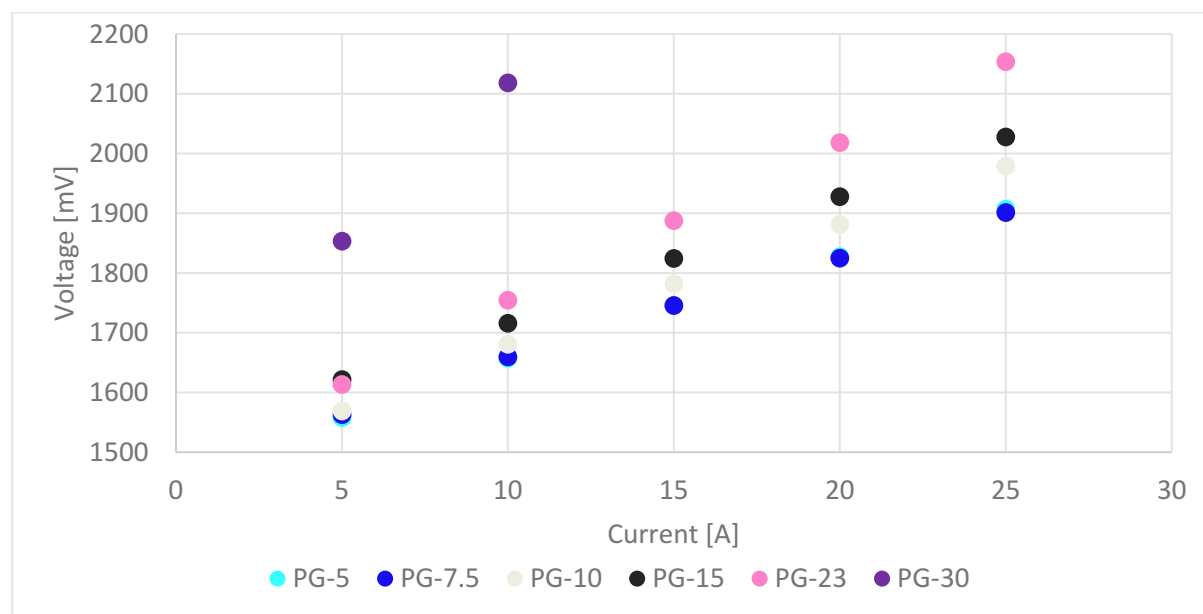
Figure 4-11: Normalised IV curves of the samples with varying ionomer content and PG as dispersion solvent.

In general, the maximum obtainable current was increased with a reduction of the ionomer content. However, a level-off effect was observed when the ionomer content was decreased to 7.5 wt%. The improved performance can be associated with the thinner film thickness of the CL and partly because of the improved pore accesibility. This effect was pronounced in samples with less than 15 wt% ionomer content as not all CL material was transferred to the membrane during hot-pressing. The biggest improvement was achieved with the PG-7.5 sample in blue, which resulted in a 24.9% lower voltage at a current density of 2 A/cm². If the series is then extrapolated, this would result in almost 4.0 A/cm² at the maximum applied voltage of 2.1 V. Otherwise, the irdium loading could even be lowered to 1.73 mg/cm² to achieve a similar obtained voltage of 2.03 V at 2 A/cm², if a linear context between the irdium loading and the performance is assumed. This represents a rather conservative assumption and the necessary irdium loading might even be lower than stated as the ohmic resistance is simultaneously decreased through the reduction of the CL's thickness. Similar current densities and considerations can be expected for the PG-5 probe in cyan. The largest drop in performance was observed between samples PG-23 in pink and PG-30 in purple, which performed at a current density of 1 A/cm² already 43.3% worse than the reference sample. All samples with an

ionomer content of 15 wt% and above (i.e. PG-23 and PG-30) showed no problems during the decal transfer, whereas PG-15 still showed an performance improvement of 11.8% at a current density of 2 A/cm² compared to the reference sample.

Figure 4-12 (see next page) depicts the comparison of the data obtained from the IV curves and how the different ink`s dispersion solvents affect the MEA performance. CHEX samples in yellow, orange and red often exceeded PG samples in grey, pink and purple, while CHEP in light and dark green performed significantly better than the two aforementioned ink formulations. However, PG-10 in grey interestingly outperformed CHEX-10 in yellow. This could be due to the inhomogeneous structure of the CHEX-10 sample as small voids covered the entire area of the printed CL. These voids are a direct result of the phobic interactions between the ink and decal foil, but only became visible after the electrodes were punched. This was not observed with the CHEX-23 samples in orange as a smooth surface was obtained. The lower dielectric constant of the dispersion solvent was the main reason why CHEX-23 an CHEP-23 outperformed the reference sample in pink. CHEP-23 in dark green showed significantly lower activation overpotentials than the other two inks with the same ionomer content (i.e. CHEX-23 and PG-23). Additionally, PG-30 samples in purple had a worse polarisation performance than CHEX-30 in red, while the testing of CHEP-30 was taken out of the scope of the work as high ionomer contents were clearly disadvantageous. Nevertheless, the CHEP-30 ink formulation is expected to result in lower voltage values than the two measured CLs with the same ionomer content of 30 wt%. The CHEP-10 ink formulation in light green resulted in the lowest observed voltage of the whole series (i.e. 1.867 V at 2 A/cm²). This is evidence for the theory that the closer the dielectric constant of the dispersion solvents is to $\varepsilon = 10$, the more uniform the dispersion of the ionomer within the ink and thus the homogeneity of the screen printed CL.
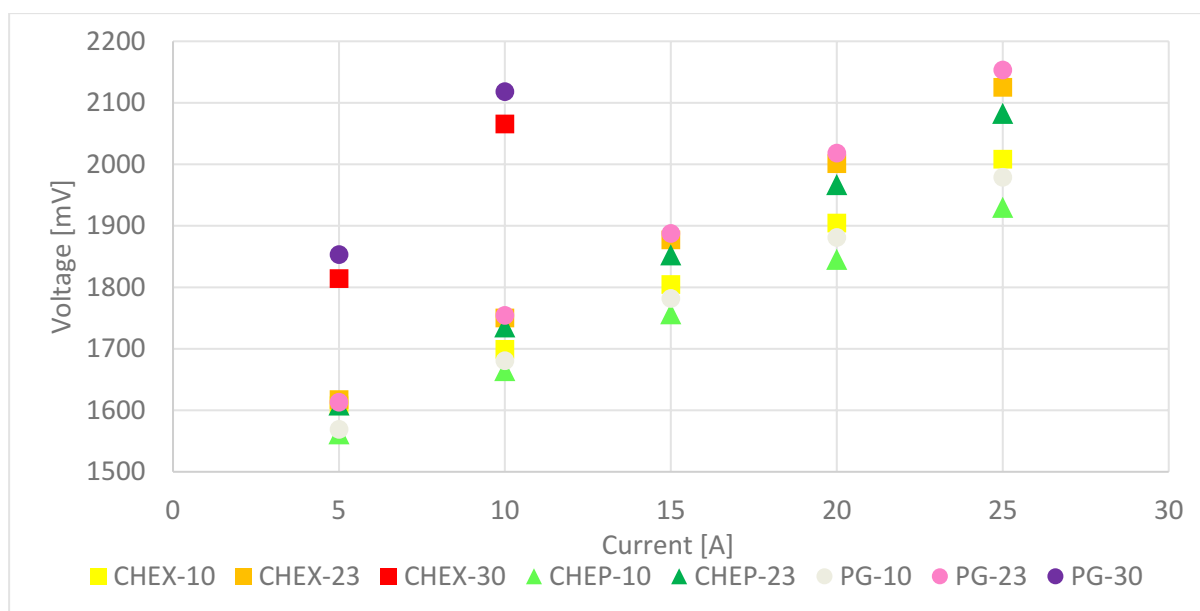
Figure 4-12: Normalised IV curves of the samples with varying ionomer content and different dispersion solvents, tested at 80 °C with a quadratic cell area of 10 cm².

Figure 4-13 (see next page) displays all ink formulations that outperformed the reference sample PG-23 in pink at a current density of 2 A/cm². This clearly shows that the decreasing ionomer content is by far more accountable for the improved polarisation performance. The flattening improvement between 7.5 and 10 wt% implies that the ideal ionomer content lies probably within this range. Compared to the ionomer influence, the different dispersion solvents are responsible for smaller performance differences, although the effects are getting more pronounced with increasing current densities. According to these findings, it appears that the solvents have a negligible influence on the optimal ionomer content. However, this could be due to the fact that these solvents have already been preselected on the basis of the catalogue of criteria used and are therefore very similar in their properties. In conclusion, the combined approach of proper solvent selection and ionomer content ultimately results in the considerable performance improvement of the CHEP-10 ink formulation in light green.
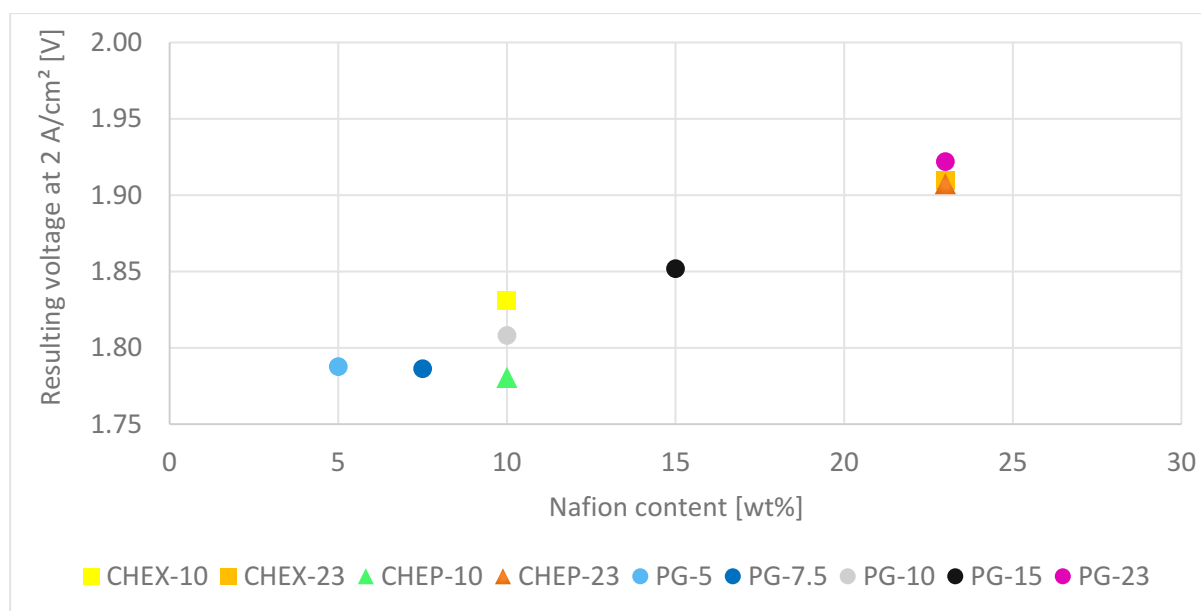
Figure 4-13: Course of the resulting voltage at a current density of 2 A/cm² in comparison to the reference sample PG-23, operation conditions are 1 bar at 80 °C.

The actual performance of the MEAs in electrolysis mode is discussed in the next section.

4.3.3 Impedance performance

The results from the EIS measurement are presented by plotting the imaginary impedance (Z'' or Z_{Im}) versus the real impedance (Z' or Z_{Re}). Thereby, the semicircle observed at high frequencies (i.e. left side of the real x-axis) corresponds to the electron transfer-limited process and a possible second semicircle at lower frequencies defines another diffusion-limited reaction mechanism. The slowest reaction mechanism is then the most remarkable one as it determines the reaction rate. It should be kept in mind that the sluggish anodic OER related losses in the impedance spectrum are usually eight times higher than the loss contribution from the cathodic HER reaction and therefore reaction rate-determining [31]. Therefore, crucial performance improvements can be achieved by focusing on optimising the anode side of the MEA.

While the left intersection with the horizontal axis Z' of the semicircle obtained at high frequencies gives the ohmic resistance, the right intersection after the subtraction of the ohmic resistance value leads to the polarisation or charge-transfer resistance. The double-layer capacitance (C_{DL}) is then calculated from the maximum of the semicircle and its corresponding frequency. Table 4-6 (see next page) gives the obtained data, wherein the PG-23 sample acts again as the reference. The best performing sample of the series was CHEP-10 as it showed an acceptable low polarisation resistance of just 5.94 mΩ and even the lowest ohmic resistance of 16.35 mΩ. However, the lowest polarisation resistance of 5.83 mΩ was achieved by CHEX-10. Furthermore, all samples close to 10 wt% ionomer content showed similar good

results. The highest C_{DL} of 725 mF was observed with CHEX-10 as it had the highest frequency peak. The PG-30 sample had the worst performance, followed closely by the CHEX-30 sample.

Sample code	Ir loading [mg/cm²]	Nafion content [wt%]	Ohmic resistance [mΩ]	Polarisation resistance [mΩ]	Capacitance [mF]
PG-5	1.66	5.02	17.80	6.58	398.0
PG-7.5	1.71	7.51	16.55	6.20	467.0
PG-10	1.83	9.96	19.00	6.00	666.5
PG-15	2.05	15.46	18.40	5.89	707.0
PG-23	2.02	23.02	23.65	6.43	423.5
PG-30	1.95	30.05	35.65	26.10	1.3
CHEX-10	2.05	10.10	17.50	5.83	725.0
CHEX-23	2.08	23.37	20.95	6.00	519.0
CHEX-30	2.42	29.95	40.95	11.15	21.8
CHEP-10	1.88	10.10	16.35	5.94	660.5
CHEP-23	1.91	22.94	20.50	6.28	375.5

Table 4-6: Ir and Nafion® content as well as essential parameters obtained from EIS measurement.

In order to illustrate the differences caused by the varied ionomer and solvent contribution onto the obtained semicircles, the y-axis was enlarged in the following EIS data figures. The undistorted Nyquist plots are given in the appendix 10.3 on page XXII for ease of comparison and clarity. The semicircle observed at high frequencies corresponds to the electron transfer limited process. If the high-frequency semicircle in the Nyquist plot has a larger diameter than the low-frequency semicircle, the slowest process is described as the rate-limiting step by the high-frequency semicircle. The results from the EIS curves therefore provide valuable indications of the areas in need of optimisation and the necessary future focus of the research scope. Furthermore, the direct comparison between the obtained EIS semicircles provides essential information about the ideal ink formulation for the anodic CL, since all other MEA components were kept constant.

Figure 4-14 (see next page) shows the EIS semicircles for all binary solvent mixtures (i.e. CHEX and CHEP samples) in the left graph and the EIS semicircles for the MEAs produced with solely PG-containing inks in the right graph. The most apparent characteristic of both graphs is that the semicircles drift further to the right with increasing ionomer content. This is especially pronounced for the depicted 30 wt% containing PG-30 in purple and in lesser extent

for the CHEX-30 sample in yellow. Both samples (i.e. PG-30 and CHEX-30) showed the highest ohmic (R_{ohm}) and polarisation resistance (R_{Pol}) of the investigated test series, as also indicated in Table 4-6 above. Contrary to the increased resistance, these samples had the lowest C_{DL} values of all samples. This is likely caused by the reduced ECSA due to the denser structure and less accessible voids. In addition, the CHEP-30 sample was not tested since it became evident that increased ionomer contents led to a significant deterioration in performance and higher ohmic overpotentials. These observations can be linked to the increased thickness of the CL and the blockage of pores within the CL. Another specific is that the EIS curve of samples with increased ionomer content contains an inflexion point resulting in an additional semicircle at lower frequencies. This is evidence for a second time dependent mechanism and the existence of more complicated types of resistances within the CL [63]. The high frequency semicircle can be attributed to the electrode/electrolyte interface, while the middle frequency semicircle corresponds to the charge transfer resistance within the CL [64, 65]. Another, yet not observed phenomenon of a 45° line would have been attributed to the fact that the resistance is increased due to the aggravated transport mechanism of the reaction products. Especially the water flow and oxygen exchange reaction are then crucially affected.
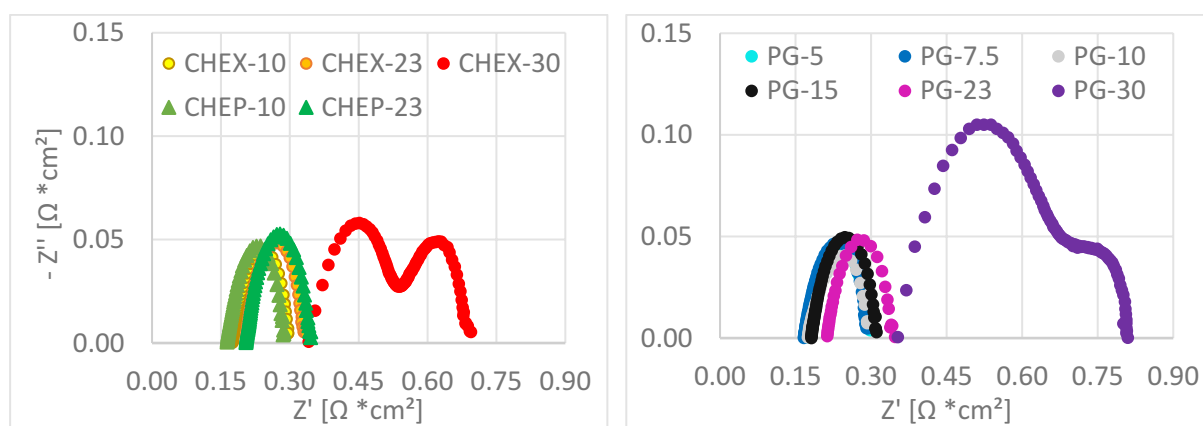
Figure 4-14: EIS semicircles illustrating the influence of the different dispersion solvents. Left: CHEX and CHEP samples; Right: PG samples. Measurements were performed at 2 A and 80 °C.

The impedance measurement at 2 A is especially useful to obtain both the magnitude of the activation overpotential and an estimation of the resulting losses. The high activation overpotential of the OER reaction is also responsible for the generally high voltage loss at low current densities. Figure 4-15 (see next page) shows decreasing resistance trends with an increase in the current range to 5 A compared to Figure 4-14 (see above).

The reduced resistance is explained by the fact that the activation overpotential is replaced by the ohmic resistance as the rate-limiting mechanism. However, this ohmic resistance is mainly

caused by the membrane not the CL itself. Therefore, more electrical current can be utilised for the production of hydrogen, as the activation overpotential has already been overcome. The area within the semicircles is reduced as the semicircles are flatter and less strongly laterally extended, which results in a higher performance compared to the cell operated at 2 A. Both the ohmic as well as the polarisation resistance are reduced and a lower capacitance is achieved as well. However, this did not change the observed order of the samples in the Nyquist plots. The best performing samples were still CHEP-10 in yellow and PG-7.5 in blue, despite the fact that hot-press transfer problems have been responsible for residues on the decals, which resulted in lower iridium loadings in the CL. The average Ir loading of CHEP-10 was 1.88 mg/cm² and only 1.71 mg/cm² for PG-7.5 respectively. This is already a promising result as the reduction of the Ir loading is one of the main objectives in PEMWE research and currently the main obstacle against the large-scale commercialisation of this hydrogen producing technology.
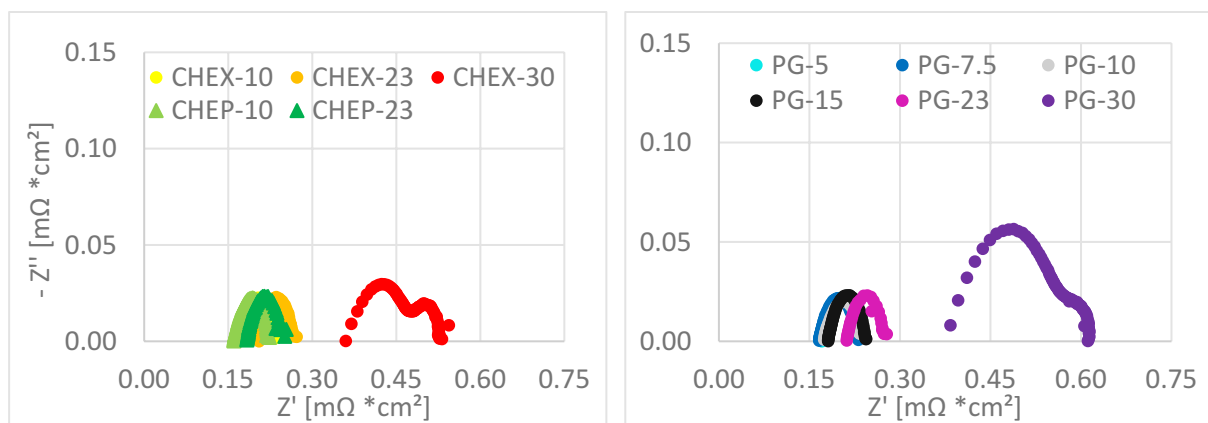
Figure 4-15: EIS curves illustrating the influence of the different dispersion solvents. Left: CHEX and CHEP samples; Right: PG samples. Measurement was performed at 5 A and 80 °C.

The dynamic behaviour of the PEMWE cell can be represented by a simplified equivalent circuit model based on EIS data, which considers the activation and ohmic losses [66]. The resistor represents the ohmic losses, accounting for the internal resistance of the PEMWE. This mainly includes the resistance of the electrodes and the protons transferred through the membrane [67]. The parallel connection of the resistor with a capacitor represents the activation losses and the double-layer charge at the interfaces between the membrane and the electrodes respectively [66]. Figure 4-16 gives two equivalent circuit models obtained for the different semicircle modes.

Figure 4-16: Equivalent circuit modelling to the obtained data. CHEX-10, CHEX-23, CHEP-10, CHEP-23, PG-10 and PG-23 data can be described with the left equivalent circuit, while CHEX-30 and PG-30 are described with the right equivalent circuit model [66, 68].

Figure 4-17 (see next page) finds that the biggest improvement was observed between samples with 30 wt% ionomer content and samples with 23 wt%. The ohmic resistance of PG-23 in pink was reduced to merely two thirds and CHEX-23 in orange even by half in comparison to the corresponding samples with the higher ionomer content. The reduction of the ionomer content resulted in a 75.4% lower polarisation resistance for PG-23 and 46.2% for CHEX-23 samples. The ionomer content has a greater influence on the EIS data than the choice of the dispersion solvent, as the appropriate amount depends largely on the pore structure of the catalyst material. In conclusion, inks containing the same ionomer content showed similar performance values.
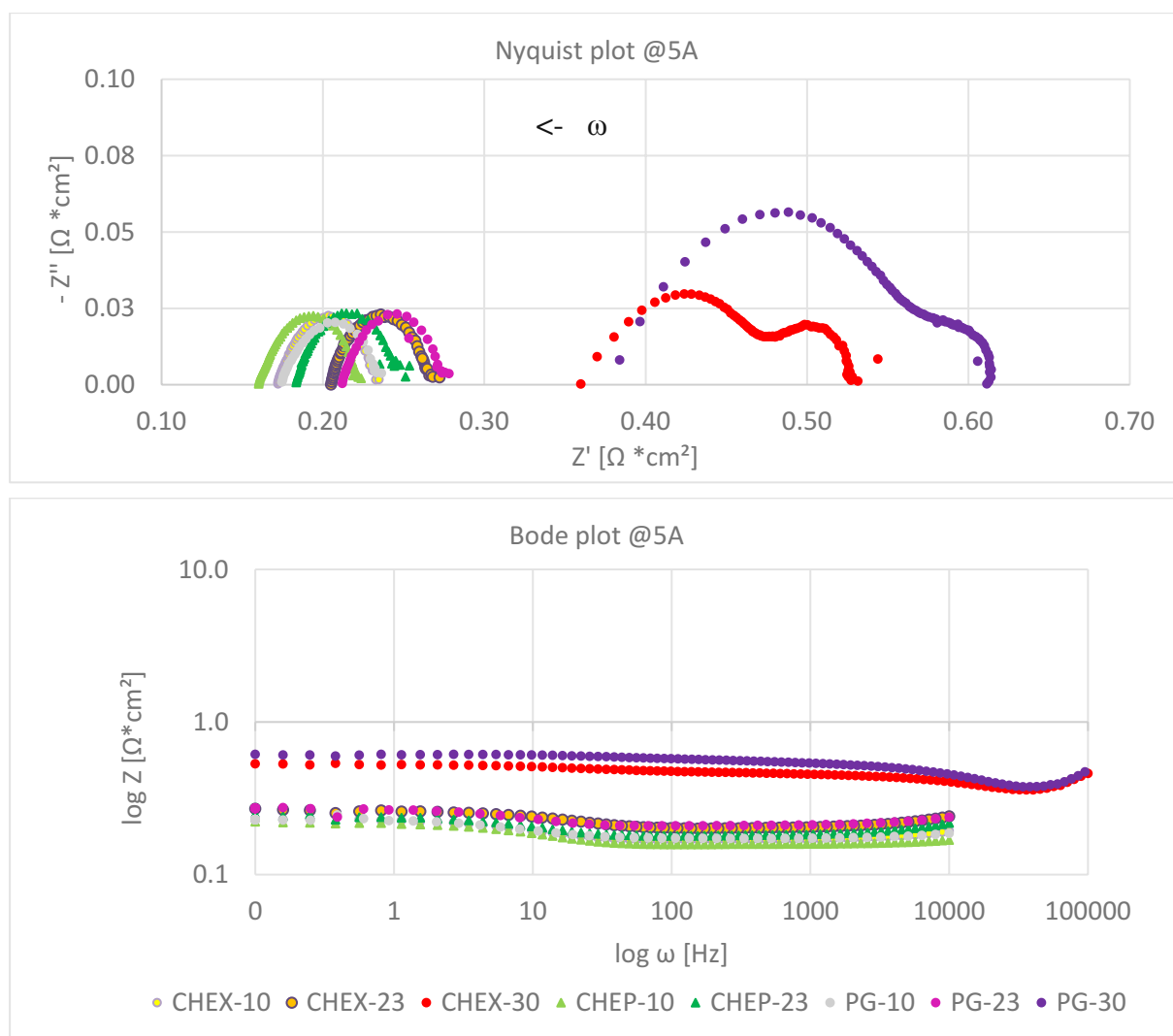
Figure 4-17: Comparison of the EIS curves in the Nyquist and Bode plot. All samples contain either 10, 23 or 30 wt% Nafion in the printed and dried CL.

Hence, the surface area of the catalyst material is the single most important parameter for the optimisation of the ionomer content. The specific surface area of the catalyst was 15 - 20 cm²/g, and therefore ink formulations containing between 7.5 - 10 wt% showed the lowest ohmic and polarisation resistance. Nevertheless, although less pronounced than the impact of the ionomer content, the solvent mixtures with CHEP and CHEX showed lower resistance values than the PG samples throughout the test series. The CHEX and PG samples revealed similar results, whereas CHEP presented the largest improvement compared to the PG samples. Therefore, it can be stated that the smaller dielectric constant of CHEP was mainly responsible for these improvements. This leads to the general assertion that solvents with a dielectric constant closer to $\varepsilon = 10$ exhibit lower internal resistance barriers than solvents with higher dielectric constants. This behaviour is likely to be caused by the advantageous distribution of the dispersed Ir nanoparticles within the applied inks. A thorough investigation of the catalyst inks would be useful to verify this hypothesis.

Now that the performance of the individual MEAs has been investigated, the next section presents another possibility of pre-estimating the performance by sampling the printed CLs on the CCM.

4.3.4 Performance prediction

The resistance of all CCMs was measured before the mount of the MEA and its respective testing. More precisely, the homogeneity of the CL was tested at least three times for each CCM with a four point-probe to obtain the average sheet resistance. The results of the lateral resistance measurement were then plotted against the Nafion® and Ir loading respectively. Figure 4-18 shows the data points obtained.
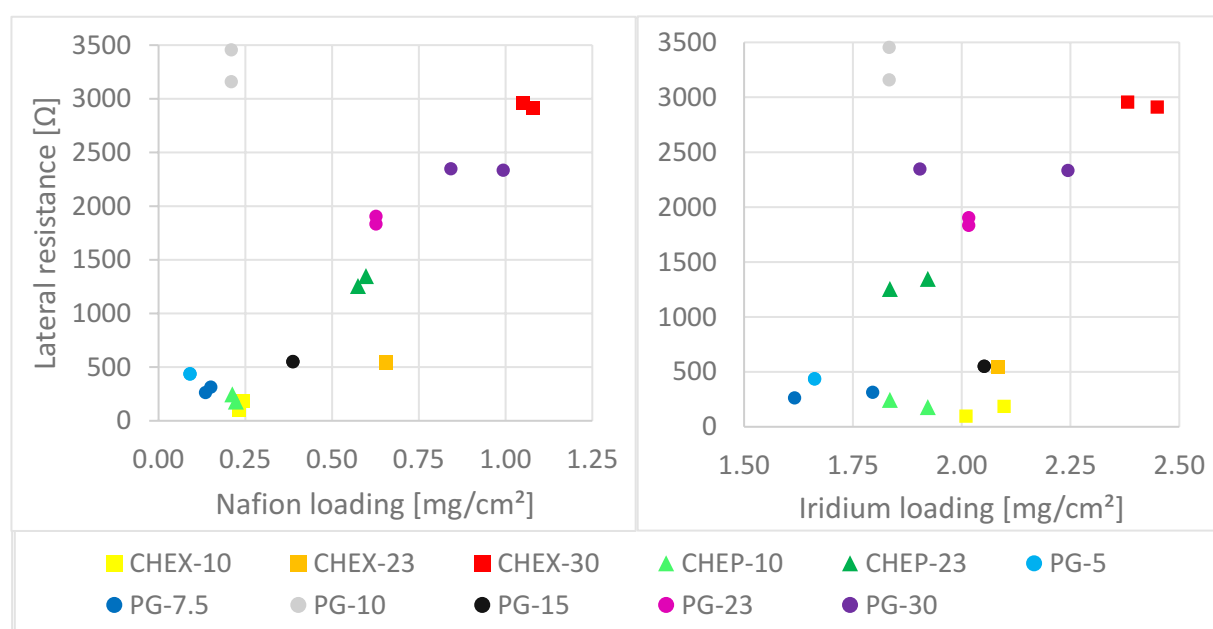
Figure 4-18: Conductivity measurement of the CCM before the MEA and operation of the cell, plotted over the Nafion and Ir loading.

As expected, inks containing a lower ionomer content had lower lateral resistance values than samples with a higher ionomer content. The lateral resistance showed values between 96 and 3,454 Ω or lateral conductivity values between 7.12 and 0.30 mS respectively. A high lateral conductivity should result in lower resistance losses during the MEA operation. Therefore, the samples of CHEX and CHEP with an ionomer content of 10 wt% had the lowest lateral resistance. Whereas for samples containing only PG as dispersion solvent, the samples with a 7.5 wt% ionomer content showed the lowest lateral resistance. An interesting outlier was observed for PG-10 samples, as these specimens resulted in the highest obtained lateral resistance values. These values occurred despite the effort that all ink formulations were prepared and printed on the same day to exclude any ink ageing effect. Unfortunately, the scope

of this work did not allow to reassess both the sample and the reason for this drastic increase in the lateral resistance. However, the elevated values had only a minor impact on the overall electrolysis performance and further investigation are required to elucidate this remarkable behaviour.

The arrangement of the measured lateral resistance is according to the data points based on a functional relationship. The data pairs from sample PG-10 were excluded from the evaluation before forming the regression line, as the outliers would result in a significantly reduced value of the coefficient of determination R^2 and a lower accuracy of the resulting trendline to the remaining measurement data. Figure 4-19 shows the obtained linear and polynomial trendlines.
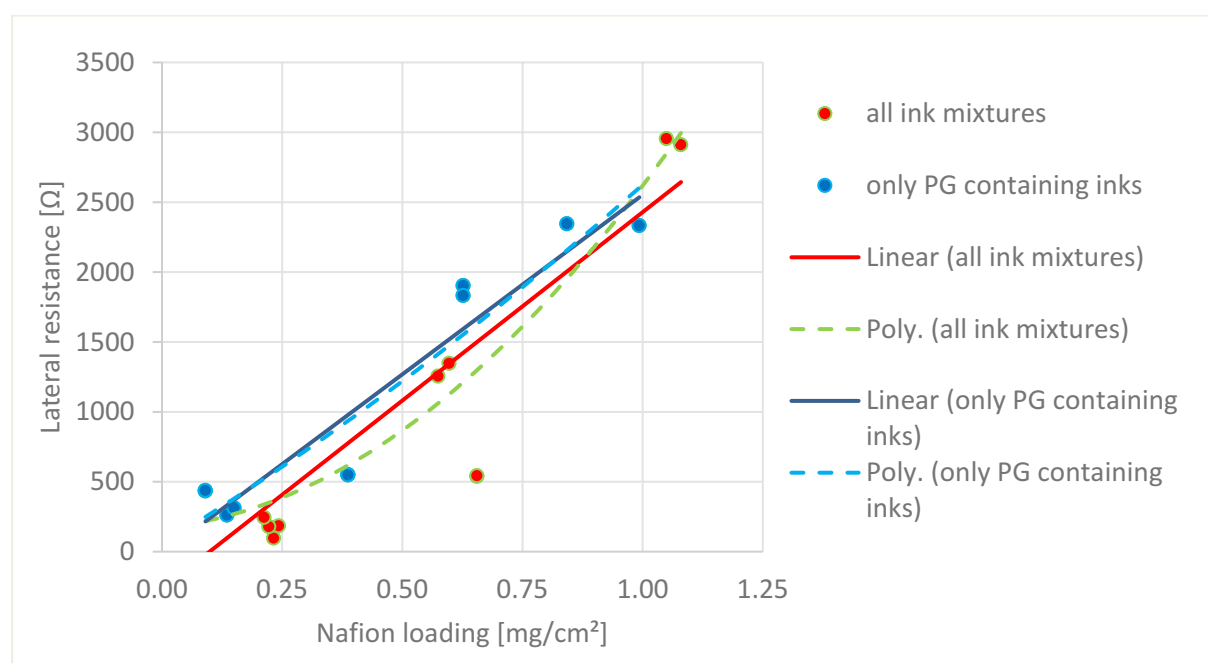
Figure 4-19: Obtained trendlines of the connection between lateral resistance and Nafion loading.

The polynomial trendline for all depicted data points is given with the equation of $y = 2109.6x^2 + 338.02x + 170.8$ and $R^2 = 0.8553$, while the linear trendline is given by $y = 2695.9x - 267.14$ and $R^2 = 0.8152$. An even higher coefficient of determination is achieved when only samples with the same dispersion solvent are used, i.e. PG with the exclusion of the PG-10 outlier. The function of the linear trendline is $y = 2568.8x - 16.038$ and $R^2 = 0.9003$. The polynomial function of the PG samples represents the correlation of the data only slightly better by $y = 482.04x^2 + 2086.6x + 55.917$ and $R^2 = 0.9023$. Therefore, the relationship between the resistance and the Nafion loading of PG inks can be expressed by a linear function.

Now that the influence of the dispersion solvent used for the ink formulation and the ionomer content in the CL on the MEA performance has been investigated, the next chapter briefly summarises the main results of this project.

5 Conclusion and Outlook

In order to achieve better performing anodic CLs for PEMWE cells, both the ink's preparation and formulation were optimised. Thereby, various ionomer and dispersion solvent mixtures were tested after a profound preselection of promising candidates. The inks obtained were screen printed onto FEP foils and hot-press transferred onto N117 membranes to obtain half-cell CCM. The CCM was combined with a PTL and a cathodic CCS to form the 5-layered MEA, which was tested in electrolysis operation. The Ir loading was targeted with values close to 2.0 mg/cm², while the commercially available GDE PtC cloth for the cathode had a Pt loading of 0.5 mg/cm².

The reproducibility of the MEA production method was demonstrated and the drying conditions were reduced to 65 °C. Nevertheless, there is still room for improvement in regard to a uniform Ir loading application per printed layer or the application of the entire ink volume as a single print layer. The exclusion of convective air flows within the drying chamber is essential to ensure a homogeneous surface structure of the CL. This further reduces or even completely prevents the extent of crack formation during the storage period. Nonetheless, the transfer from the decals to the membrane forming the CCM should be carried out as quickly as possible to completely avoid any disruptions that may occur due to cracking.

The ionomer content of the CL was found to play a significant role in both performance and transferability from the decals. The content should therefore be adjusted to the catalyst's ECSA to achieve significantly improved mass exchange rates and high proton conductivity. A binary mixture of 50:50 weight percent of cycloheptanol/propylene glycol proved to be the best performing dispersion solvent. Furthermore, the highest activity was found for samples with an ionomer content of 10 wt% in the dried CL. All samples with an ionomer content of 15 wt% and above were highly reproducible, whereas samples with a lower ionomer content showed problems with complete transferability from the FEP decals to the membrane. The problem increased further with decreasing ionomer content. This means that the optimal ionomer content lies within a range of 10 - 15 wt%, as long as an indirect decal transfer process and the Ir black powder with a surface area of about 15 m²/g is used for the ink formulation.

Samples with cyclohexanol outperformed the reference material, but the prepared inks must be stored constantly at 25 °C to prevent premature solidification. If these process conditions are maintained, these inks represent a good alternative to PG-containing inks.

The best performing sample was CHEP-10, which reached a potential of 1.867 V at 2 A/cm² with an Ir loading of 1.88 mg/cm² within the CL. This performance was already maintained over several days and enables an effective reduction of the iridium content. Moreover, the achieved current output of the mass-averaged IV potential was 37.29% higher for sample CHEP-10 compared to the reference sample PG-23. The best performing sample with only PG as dispersion solvent had an ionomer content of 7.5 wt% in the dried CL. Nevertheless, the choice should not only be based on the performance but also on reproducibility, so samples containing 15 wt% ionomer content constitute a good trade-off.

Future research should also include the influence of the supported catalyst materials on the observed process conditions and the optimal ionomer content. In any case, the ionomer content is significantly affected by the porosity and specific surface area of the supported catalyst materials. More complex dispersion solvent mixtures with three or more components may be analysed and optimised to achieve beneficial physicochemical properties of the ink. Further improvements for the described process include that the ink could be transferred directly to the membrane in order to completely eliminate the transfer problematic and speed up the production process. However, the direct production process for obtaining CCMs is likely to be negatively affected by swelling processes induced to a certain degree by the different structures of the dispersion solvent or by the duration of the drying time. An appropriate choice of solvent based on a suitable catalogue of criteria would be advisable. Additionally, accelerated stress tests and longer operation times could be performed to further access the inks' suitability for the usage in large-scale PEMWEs and to obtain the long-term electrochemical degradation behaviour of the manufactured MEAs.

6 References

[1] J. Abe, A. Popoola, E. Ajenifuja and O. Popoola, "Hydrogen energy, economy and storage: Review and recommendation," *International Journal of Hydrogen Energy,* vol. 44, no. 29, pp. 15072-15086, 2019.

[2] A. Borgschulte, "The Hydrogen Grand Challenge," *Frontiers in Energy Research,* vol. 4, no. 11, pp. 1-8, 2016.

[3] IEA, "The Future of Hydrogen: Seizing today's opportunities," IEA publications, Paris, 2019.

[4] J. E. Park, S. Kim, O.-H. Kim, C.-Y. Ahn, M.-J. Kim, S. Y. Kan, T. I. Jeon, J.-G. Shim, D. Lee, J. H. Lee, Y.-H. Cho and Y.-E. Sung, "Ultra-low loading of IrO2 with an inverse-opal structure in a polymer-exchange membrane water electrolysis," *Nano Energy,* vol. 58, p. 158–166, 2019.

[5] L. Bertuccioli, A. Chan, D. Hart, F. Lehner, B. Madden and E. Standen, "Development of Water Electrolysis in the European Union," E4tech Sàrl and Element Energy Ltd, Cambridge (UK), Lausanne (CH), 2014.

[6] M. Carmo, D. L. Fritz, J. Mergel and D. Stolten, "A comprehensive review on PEM water electrolysis," *International Journal of Hydrogen Energy,* vol. 38, no. 12, pp. 4901-4934, 2013.

[7] X. Wu, K. Scott and V. Puthiyapura, "Polymer electrolyte membrane water electrolyser with Aquivion® short side chain perfluorosulfonic acid ionomer binder in catalyst layers," *International Journal of Hydrogen Energy,* vol. 37, no. 18, pp. 13243-13248, 2012.

[8] M. Bernt and H. A. Gasteiger, "Influence of Ionomer Content in IrO2/TiO2 Electrodes on PEM Water Electrolyzer Performance," *Journal of The Electrochemical Society,* vol. 163, no. 11, pp. F3179-F3189, 2016.

[9] W. Xu and K. Scott, "The effects of ionomer content on PEM water electrolyser membrane electrode assembly performance," *International Journal of Hydrogen Energy,* vol. 35, no. 21, pp. 12029-12037, 2010.

[10] K. Wuttikid, N. Worayos and K. Punyawudho, "Analysis of Catalyst Ink Compositions for Fabricating Membrane Electrode Assemblies in PEM Fuel Cells," *CMU J. Nat. Sci.,* vol. 16, no. 4, pp. 275-281, 2017.

[11] F. Hegge, R. Moroni, P. Trinke, B. Bensmann, R. Hanke-Rauschenbach, S. Thiele and S. Vierrath, "Three-dimensional microstructure analysis of a polymer electrolyte membrane water electrolyzer anode," *Journal of Power Sources,* vol. 393, pp. 62-66, 2018.

[12] J. Majasan, J. I. S. Cho, M. Maier, I. Dedigama, P. R. Shearing and D. Brett, "Effect of Anode Flow Channel Depth on the Performance of Polymer Electrolyte Membrane Water Electrolyser," *ECS Transactions,* vol. 85, no. 13, pp. 1593-1603, 2018.

[13] M. M. Rashid, M. K. A. Mesfer, H. Naseem and M. Danish, "Hydrogen Production by Water Electrolysis: A Review of Alkaline Water Electrolysis, PEM Water Electrolysis and High Temperature Water Electrolysis," *International Journal of Engineering and Advanced Technology ,* vol. 4, no. 3, pp. 80-93, 2015.

[14] M. Bernt, A. Siebel and H. A. Gasteiger, "Analysis of Voltage Losses in PEM Water Electrolyzers with Low Platinum Group Metal Loadings," *Journal of The Electrochemical Society,* vol. 165, no. 5, pp. F305-F314, 2018.

[15] U. Babic, M. Suermann, F. N. Büchi, L. Gubler and T. J. Schmidt, "Review - Identifying Critical Gaps for Polymer Electrolyte Water Electrolysis Development," *Journal of The Electrochemical Society,* vol. 164, no. 4, pp. F387-F399, 2017.

[16] J. Kai, R. Saito, K. Terabaru, H. Li, H. Nakajima and K. Ito, "Effect of Temperature on the Performance of Polymer Electrolyte Membrane Water Electrolysis: Numerical Analysis of Electrolysis Voltage Considering Gas/Liquid Two-Phase Flow," *Journal of The Electrochemical Society,* vol. 166, no. 4, pp. F246-F254 , 2019.

[17] S. Siracusano, V. Baglio, N. V. Dijk, L. Merlo and A. S. Aricò, "Enhanced performance and durability of low catalyst loading PEM water electrolyser based on a short-side chain perfluorosulfonic ionomer," *Applied Energy,* vol. 192, pp. 477-489, 2017.

[18] B. J. Bladergroen, H. Su, S. Pasupathi and V. Linkov, "Overview of Membrane Electrode Assembly Preparation Methods for Solid Polymer Electrolyte Electrolyzer," in *Electrolysis*, Rijeka, InTech, 2012, pp. 45-61.

[19] P. E. Santangelo, M. Cannio and M. Romagnoli, "Review of Catalyst-deposition Techniques for PEMFC Electrodes," *Tecnica Italiana-Italian Journal of Engineering Science,* vol. 63, no. 1, pp. 65-72, 2019.

[20] R. Kumari and V. Kumar, "Impact of zinc doping on structural, optical, and electrical properties of CdO films prepared by sol–gel screen printing mechanism," *Journal of Sol-Gel Science and Technology,* vol. 94, p. 648–657, 2020.

[21] M. R. Hill, "Preparation of catalyst coated membranes using screen printing," University of Cape Town, Cape Town, 2013.

[22] T. M. R. Lagarteira, "MEAs preparation via wet routes for PEM electrolysis," Universidade do Porto, Köln; Porto, 2016.

[23] S. Pasupathi, H. Su, H. Liang and B. G. Pollet, "Advanced Technologies for Proton-Exchange Membrane Fuel Cells," in *Electrochemical Energy: Advanced Materials and Technologies*, Boca Raton, CRC Press, 2017.

[24] B. G. Pollet, Power Ultrasound in Electrochemistry: From Versatile Laboratory Tool to Engineering Solution, Chichester: John Wiley & Sons, Ltd, 2012.

[25] B. G. Pollet and J. T. Goh, "The importance of ultrasonic parameters in the preparation of fuel cell catalyst inks," *Electrochimica Acta,* vol. 128, pp. 292-303, 2014.

[26] M. Adamski, N. Peressin, S. Holdcroft and B. G. Pollet, "Does power ultrasound affect Nafion® dispersions?," *Ultrasonics - Sonochemistry,* vol. 60, 2020.

[27] I. Takahashi and S. Kocha, "Examination of the activity and durability of PEMFC catalysts in liquid electrolytes," *Journal of Power Source,* vol. 195, no. 19, pp. 6312-6322, 2010.

[28] B. G. Pollet, "The Use of Power Ultrasound for the Production of PEMFC and PEMWE Catalysts and Low-Pt Loading and High-Performing Electrodes," *Catalysts,* vol. 9, no. 3, 2019.

[29] H. Lyu, B. Gao, F. He, C. Ding, J. Tang and J. C. Crittenden, "Ball-Milled Carbon Nanomaterials for Energy and Environmental Applications," *ACS Sustainable Chem. Eng.,* vol. 5, no. 11, pp. 9568-9585, 2017.

[30] C. F. Burmeister and A. Kwade, "Process engineering with planetary ball mills," *Chemical Society Reviews,* vol. 42, no. 18, pp. 7660-7667, 2013.

[31] C. Rozain and P. Millet, "Electrochemical characterization of Polymer Electrolyte MembraneWater Electrolysis Cells," *Electrochimica Acta,* vol. 131, p. 160–167, 2014.

[32] J. Wu, X. Z. Yuan, H. Wang, M. Blanco, J. J.Martin and J. Zhang, "Diagnostic tools in PEM fuel cell research: Part I Electrochemical techniques," *International Journal of Hydrogen Energy,* vol. 33, no. 6, pp. 1735-1746, 2008.

[33] E. T. Ojong, J. T. H. Kwan, A. Nouri-Khorasani, A. Bonakdarpour, D. P. Wilkinson and T. Smolinka, "Development of an experimentally validated semi-empirical fully-coupled performance model of a PEM electrolysis cell with a 3-D structured porous transport layer," *International Journal of Hydrogen Energy,* vol. 42, no. 41, pp. 25831-25847, 2017.

[34] J. v. d. Merwe, K. Uren, G. v. Schoor and D. Bessarabov, "Characterisation tools development for PEM electrolysers," *International Journal of Hydrogen Energy,* vol. 39, no. 26, pp. 14212-14221, 2014.

[35] Z. Qi, "Electrochemical methods for catalyst activity evaluation," in *PEM Fuel Cell Electrocatalysts and Catalyst Layers: Fundamentals and Applications*, London, Springer, 2008, pp. 547-607.

[36] R. O'Hayre, S.-W. Cha, W. Colella and F. B. Prinz, Fuel Cell Fundamentals, New York: Wiley, 2006.

[37] N. Zamel, "The catalyst layer and its dimensionality – A look into its ingredients and how to characterize their effects," *Journal of Power Sources,* vol. 309, pp. 141-159, 2016.

[38] T. Malkow, A. Pilenga and G. Tsotridis, "EU harmonised test procedure: electrochemical impedance spectroscopy for water electrolysis cells," Publications Office of the European Union, Luxembourg, 2018.

[39] H. A. El-Sayed, A. Weiß, L. F. Olbrich, G. P. Putro and H. A. Gasteiger, "OER Catalyst Stability Investigation Using RDE Technique; A Stability Measure or an Artifact?," *Journal of The Electrochemical Society,* vol. 166, no. 8, pp. F458-F464, 2019.

[40] N. Elgrishi, K. J. Rountree, B. D. McCarthy, E. S. Rountree, T. T. Eisenhart and J. L. Dempsey, "A Practical Beginner's Guide to Cyclic Voltammetry," *Journal of Chemical Education,* vol. 95, pp. 197-206, 2018.

[41] C. Du, Q. Tan, G. Yin and J. Zhang, "Rotating Disk Electrode Method," in *Rotating Electrode Methods and Oxygen Reduction Electrocatalysts*, Amsterdam, Elsevier, 2014, pp. 171-198.

[42] K. Karan, "Determination of CL Ionomer Conductivity," *ECS Transactions,* vol. 50, no. 2, pp. 395-403, 2013.

[43] M. Thommes, K. Kaneko, A. V. Neimark, J. P. Olivier, F. Rodriguez-Reinoso, J. Rouquerol and K. S. W. Sing, "Physisorption of gases, with special reference to the

evaluation of surface area and pore size distribution (IUPAC Technical Report)," *Pure and Applied Chemistry,* vol. 87, no. 9-10, p. 1051–1069, 2015.

[44] P. Lettenmeier, L. Wang, U. Golla-Schindler, P. Gazdzicki, N. A. Cañas, M. Handl, R. Hiesgen, S. S. Hosseiny, A. S. Gago and K. A. Friedrich, "Nanosized IrOx–Ir Catalyst with Relevant Activity for Anodes of Proton Exchange Membrane Electrolysis Produced by a Cost-Effective Procedure," *Angewandte Chemie International Edition,* vol. 55, no. 2, pp. 742-746, 2016.

[45] H. Yu, L. Bonville, J. Jankovic and R. Maric, "Microscopic insights on the degradation of a PEM water electrolyzer with ultra-low catalyst loading," *Applied Catalysis B: Environmental,* vol. 260, 2020.

[46] A. Orfanidi, P. J. Rheinländer, N. Schulte and H. A. Gasteiger, "Ink Solvent Dependence of the Ionomer Distribution in the Catalyst Layer of a PEMFC," *Journal of The Electrochemical Society,* vol. 165, no. 14, pp. F1254-F1263, 2018.

[47] P. Kúš, Thin-Film Catalysts for Proton Exchange Membrane Water Electrolyzers and Unitized Regenerative Fuel Cells, Prague: Springer International Publishing, 2019.

[48] K. M. Koczkur, S. Mourdikoudis, L. Polavarapu and S. E. Skrabalak, "Polyvinylpyrrolidone (PVP) in nanoparticle synthesis," *Dalton Transactions,* vol. 44, no. 41, pp. 17883-17905, 2015.

[49] J. Newton, J. A. Preece and B. G. Pollet, "Control of nanoparticle aggregation in PEMFCs using surfactants," *International Journal of Low-Carbon Technologies,* vol. 7, no. 1, pp. 38-43, 2012.

[50] H. Ohno, S. Nohara, K. Kakinuma, M. Uchida and H. Uchida, "Effect of Electronic Conductivities of Iridium Oxide/Doped SnO2 Oxygen-Evolving Catalysts on the Polarization Properties in Proton Exchange Membrane Water Electrolysis," *Catalysts,* vol. 9, no. 74, pp. 1-12, 2019.

[51] S.-B. Han, Y.-H. Mo, Y.-S. Lee, S.-G. Lee, D.-H. Park and K.-W. Park, "Mesoporous iridium oxide/Sb-doped SnO2 nanostructured electrodes for polymer electrolyte membrane water electrolysis," *International Journal of Hydrogen Energy,* vol. 45, no. 3, pp. 1409-1416, 2020.

[52] O. Lori and L. Elbaz, "Advances in Ceramic Supports for Polymer Electrolyte Fuel Cells," *Catalysts,* vol. 5, no. 3, pp. 1445-1464, 2015.

[53] Z. Huang, R. Lin, R. Fan, Q. Fan and J. Ma, "Effect of TiB2 Pretreatment on Pt/TiB2 Catalyst Performance," *Electrochimica Acta,* no. 139, p. 48–53, 2014.

[54] S. Yin, S. Mu, H. Lv, N. Cheng, M. Pan and H. Wang, "A highly stable catalyst for PEM fuel cell based on durable titanium diboride support and polymer stabilization," *Applied Catalysis B Environmental,* vol. 93, no. 3-4, pp. 233-240, 2010.

[55] S. Yin, S. Mu, M. Pan and Z. Fu, "A highly stable TiB2-supported Pt catalyst for polymer electrolyte membrane fuel cells," *Journal of Power Sources,* vol. 196, no. 19, pp. 7931-7936, 2011.

[56] J. Juodkazytė, B. Šebeka, I. Valsiunas and K. Juodkazis, "Iridium Anodic Oxidation to Ir(III) and Ir(IV) Hydrous Oxides," *Electroanalysis,* vol. 17, no. 11, pp. 947-952, 2005.

[57] W. Wang, S. Chen, J. Li and W. Wang, "Fabrication of catalyst coated membrane with screen printing method in a proton exchange membrane fuel cell," *International Journal of Hydrogen Energy,* vol. 40, no. 13, pp. 4649-4658, 2015.

[58] C. Welch, A. Labouriau, R. Hjelm, B. Orler, C. Johnston and Y. S. Kim, "Nafion in Dilute Solvent Systems: Dispersion or Solution?," *ACS Macro Lett.,* vol. 1, no. 12, pp. 1403-1407, 2012.

[59] Engineering ToolBox, "Engineering ToolBox: Dynamic Viscosity of common Liquids," 2001. [Online]. Available: https://www.engineeringtoolbox.com/. [Accessed July 2020].

[60] National Institutes of Health, "PubChem," National Center for Biotechnology Information, 2004. [Online]. Available: https://pubchem.ncbi.nlm.nih.gov/. [Accessed 2020].

[61] M. Dixit and K. Hatzell, "Understanding Binary Interactions and Aging Effects in Catalyst Layer Inks for Controlled Manufacturing," *ECS Transactions,* vol. 80, no. 8, pp. 301-307, 2017.

[62] T. Böhm, R. Moroni, M. Breitwieser, S. Thiele and S. Vierrath, "Spatially Resolved Quantification of Ionomer Degradation in Fuel Cells by Confocal Raman Microscopy," *Journal of The Electrochemical Society,* vol. 166, no. 7, pp. F3044-F3051, 2019.

[63] E. Fontananova, "Impedance Spectroscopy, Membrane Characterization," in *Encyclopedia of Membranes*, Berlin, Heidelberg, Springer-Verlag, 2014.

[64] N. Effendi, N. Samsi, S. Zawawi, O. Hassan, R. Zakaria, M. Yahya and A. Ali, "Studies on Graphene Zinc-Oxide Nanocomposites Photoanodes for High-Efficient Dye-Sensitized Solar Cells," *AIP Conference Proceedings,* no. 1, 2017.

[65] J. Chen, C. Li, D. Zhao, W. Lei, Y. Zhang, M. Cole, D. Chu, B. Wang, Y. Cui, X. Sun and W. Milne, "A quantum dot sensitized solar cell based on vertically aligned carbon nanotube templated ZnO arrays," *Electrochemistry Communications,* vol. 12, no. 10, pp. 1432-1435, 2010.

[66] W.-Y. Chang, "Estimating equivalent circuit parameters of proton exchange membranefuel cell using the current change method," *International Journal of Electrical Power & Energy Systems,* vol. 53, pp. 584-591, 2013.

[67] U.Reggiani, L.Sandrolini and G. Burbui, "Modelling a PEM fuel cell stack with a nonlinear equivalent circuit," *Journal of Power Sources,* vol. 165, no. 1, pp. 224-231, 2007.

[68] O. Atlam and M. Kolhe, "Equivalent electrical model for a proton exchange membrane (PEM) electrolyser," *Energy Conversion and Management,* vol. 52, no. 5-9, pp. 2952-2957, 2011.

7 List of Figures

8 List of Tables

9 List of Symbols

Symbol	Units	Description
a_s	$m^2\ kg^{-1}$	specific surface area
C	-	shape factor of the isotherm
E	V	electrode potential
E_a	V	activation overpotential
E_{cell}	V	cell potential
E_m	V	mass transfer overpotential
E_o	V	ohmic overpotential
E_r	V	reversible potential
F	$C\ mol^{-1}$	Faraday`s number
G	J	Gibbs free energy
G_0	J	standard Gibbs free energy
H	J	enthalpy
I	A	current
i	-	imaginary unit
I_{AC}	A	AC current
j	$A\ m^{-2}$	current density
j_o	$A\ m^{-2}$	exchange current density
K	-	equilibrium constant
m	kg	mass of adsorbent
n	mol	amount of adsorbent
N_A	mol^{-1}	Avogadro constant
n_m	mol	monolayer capacity
p	$N\ m^{-2}$	equilibrium partial pressure
R	$J\ mol^{-1}\ K^{-1}$	gas law constant
R	$V\ A^{-1}$	resistance
S	$J\ K^{-1}$	entropy
T	K	temperature
U_{AC}	V	AC voltage
z	-	charge number

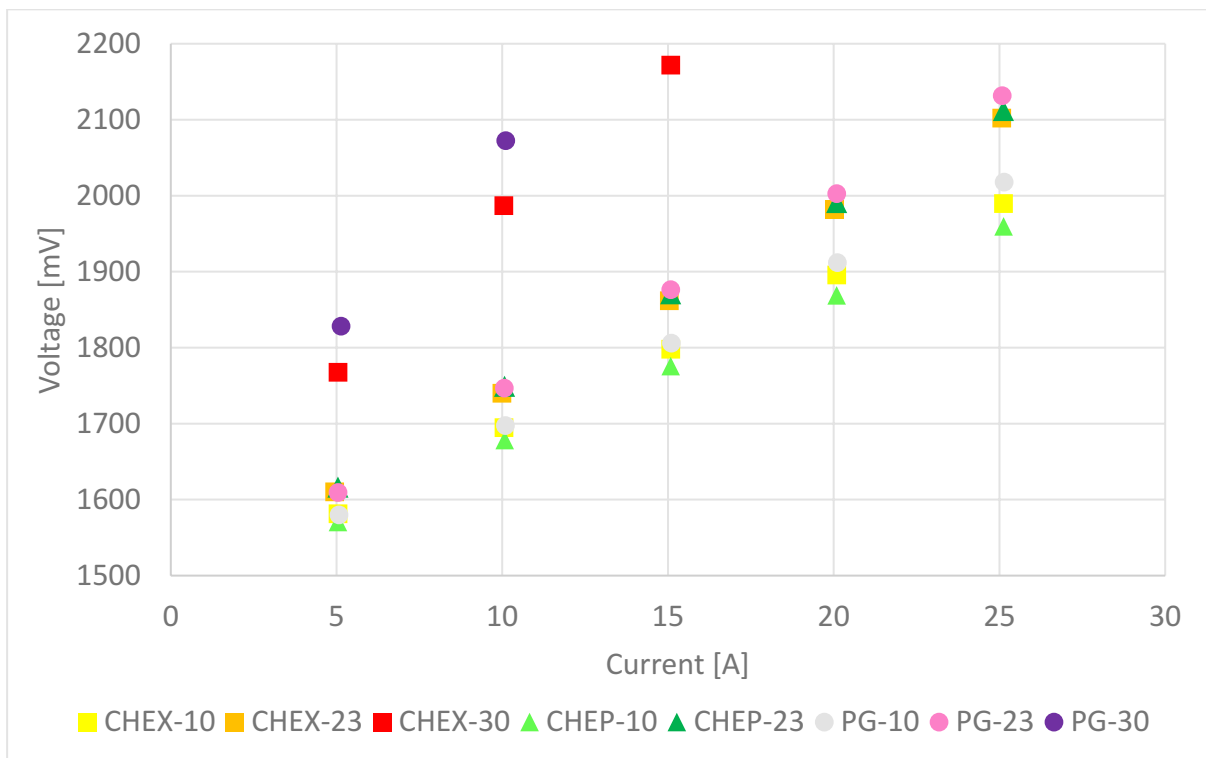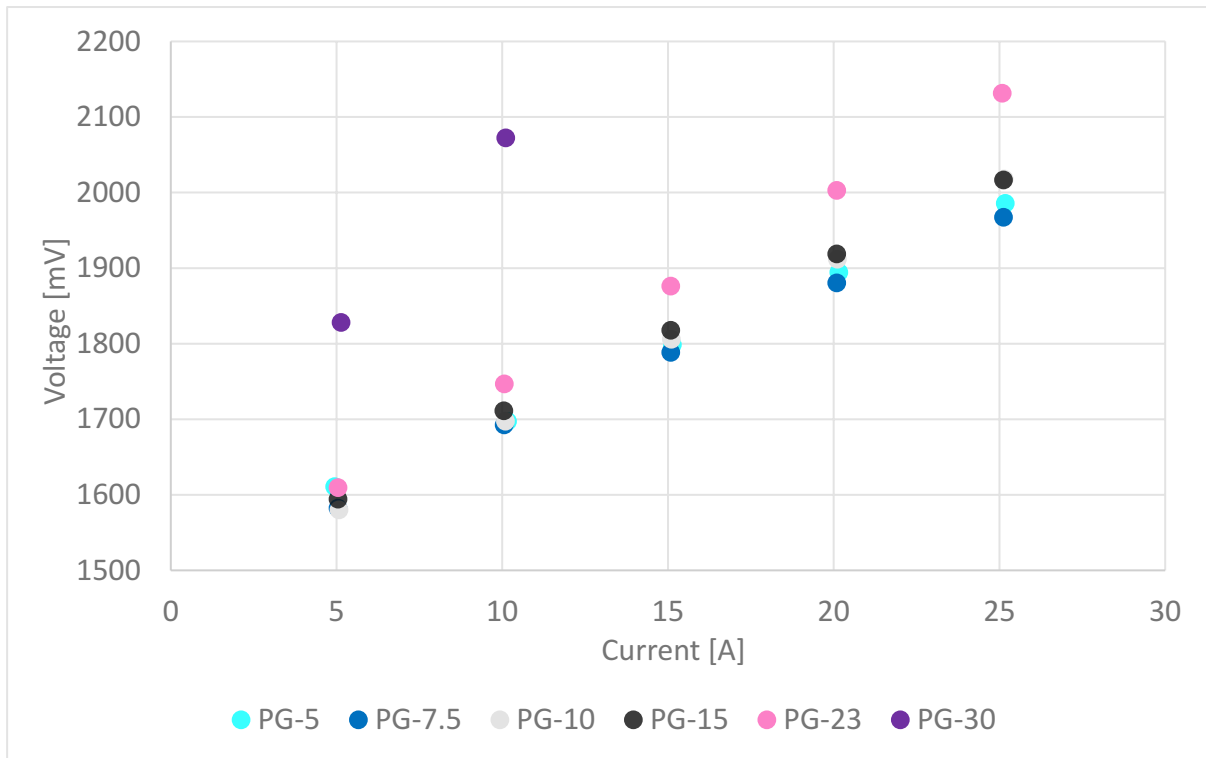|		
Z	V A^{-1}	impedance
α_a, α_{ox}	-	anodic charge transfer coefficient
α_c, α_{red}	-	cathodic charge transfer coefficient
η	-	thermodynamic efficiency
θ	-	phase difference
σ_m	m^2	molecular cross-sectional area
ϕ	-	phase shift

10 Appendix

10.1 Conditioning
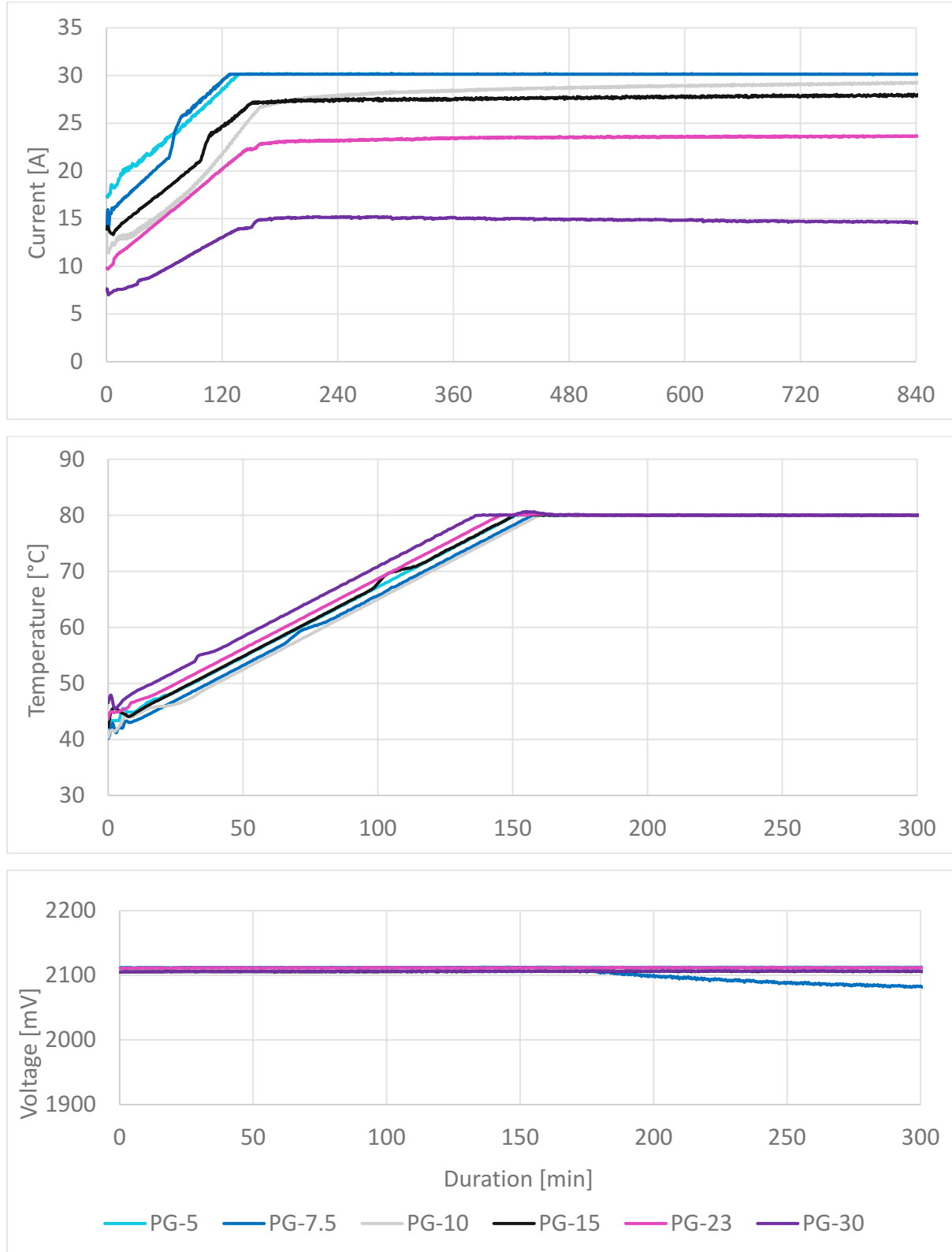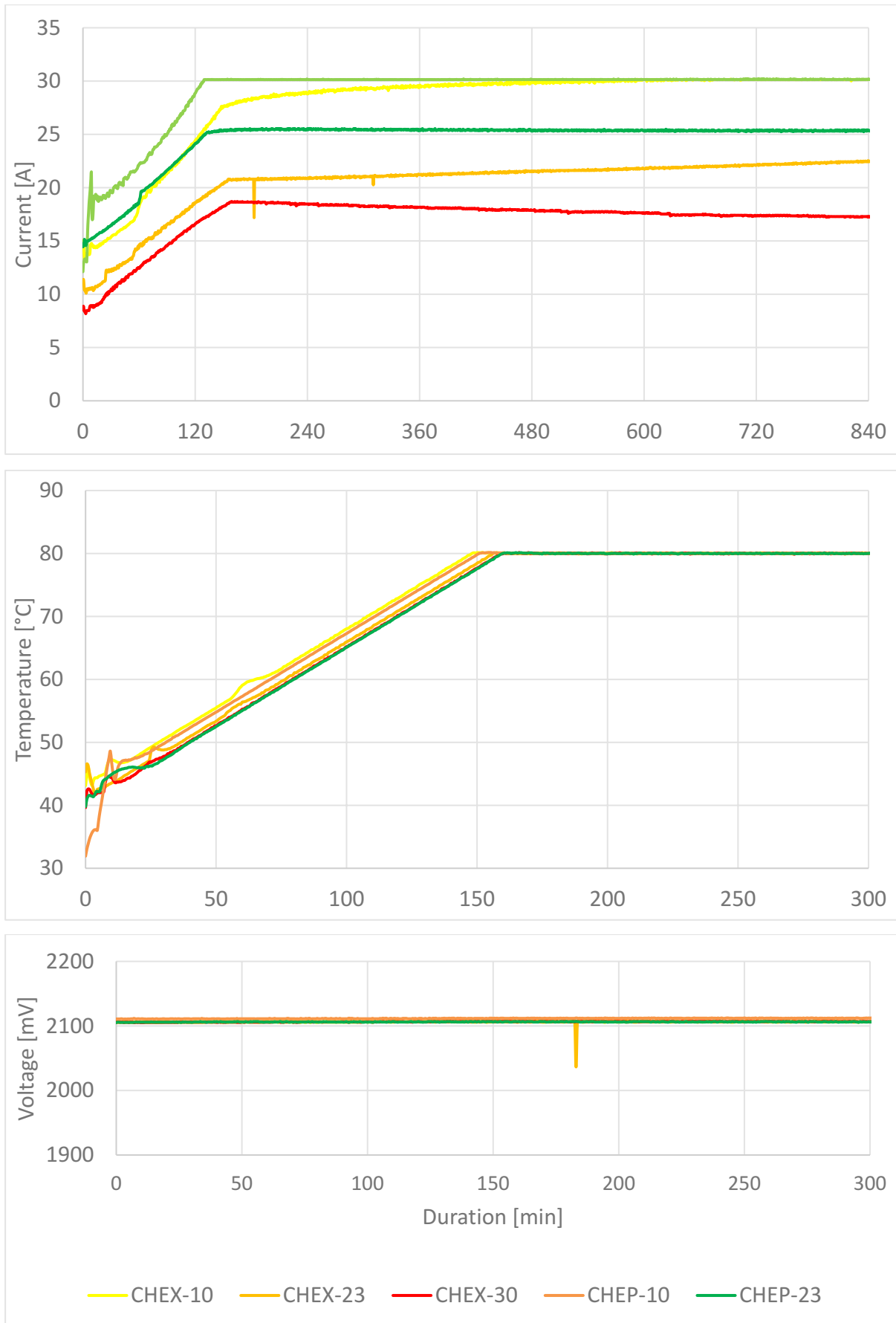
10.2 IV graphs

10.3   Nyquist plots

Nyquist plot @2A

○ CHEX-10 ○ CHEX-23 ● CHEX-30 ▲ CHEP-10 ▲ CHEP-23

Nyquist plot @2A

● PG-5 ● PG-7.5 ● PG-10 ● PG-15 ● PG-23 ● PG-30

Nyquist plot @5A

Legend: CHEX-10, CHEX-23, CHEX-30, CHEP-10, CHEP-23

Nyquist plot @5A

Legend: PG-5, PG-7.5, PG-10, PG-15, PG-23, PG-30